

Star Formation History in Barred Spiral Galaxies. AGN Feedback

Fidèle Robichaud,^{1,2} David Williamson,^{1,2} Hugo Martel,^{1,2} Daisuke Kawata,³ and Sara L. Ellison⁴

¹*Département de physique, de génie physique et d'optique, Université Laval, Québec, QC, G1V 0A6, Canada*

²*Centre de Recherche en Astrophysique du Québec, QC, Canada*

³*Mullard Space Science Laboratory, University College London, Holmbury St Mary, Dorking, Surrey, UK*

⁴*Department of Physics and Astronomy, University of Victoria, Victoria, BC, Canada*

Accepted XXX. Received XXX; in original form XXX

ABSTRACT

We present a numerical study of the impact of AGN accretion and feedback on the star formation history of barred disc galaxies. Our goal is to determine whether the effect of feedback is positive (enhanced star formation) or negative (quenched star formation), and to what extent. We performed a series of 12 hydrodynamical simulations of disc galaxies, 10 barred and 2 unbarred, with various initial gas fractions and AGN feedback prescriptions. In barred galaxies, gas is driven toward the centre of the galaxy and causes a starburst, followed by a slow decay, while in unbarred galaxies the SFR increases slowly and steadily. AGN feedback suppresses star formation near the central black hole. Gas is pushed away from the black hole, and collides head-on with inflowing gas, forming a dense ring at a finite radius where star formation is enhanced. We conclude that both negative and positive feedback are present, and these effects mostly cancel out. There is no net quenching or enhancement in star formation, but rather a displacement of the star formation sites to larger radii. In unbarred galaxies, where the density of the central gas is lower, quenching of star formation near the black hole is more efficient, and enhancement of star formation at larger radii is less efficient. As a result, negative feedback dominates. Lowering the gas fraction reduces the star formation rate at all radii, whether or not there is a bar or an AGN.

Key words: galaxies: active – galaxies: evolution – galaxies: spiral – stars: formation

1 INTRODUCTION

The existence of tight relations between the mass of supermassive black holes (SBH) producing Active Galactic Nuclei (AGN), the velocity dispersion of their hosts galaxies (Ferrarese & Merritt 2000; Gebhardt et al. 2000; Gültekin et al. 2009), and the bulge stellar mass (Marconi & Hunt 2003; Häring & Rix 2004; McConnell & Ma 2013) strongly suggests that AGN and their host do not evolve independently. AGN deposit large amounts of energy into the surrounding interstellar medium (ISM), and this energy might be sufficiently large to accelerate the gas above the escape velocity and generate a galactic wind that will deposit energy and metal-enriched gas into the intergalactic medium. This greatly affects the star formation histories of the host galaxies. Star formation in galaxies is a highly inefficient process. The baryon density parameter Ω_{b0} , estimated from the cosmic abundance of light elements, is of order 0.04 (Kirkman et al. 2003). By contrast, estimates of the average stellar mass density give

$\rho_* \simeq 5.6 \times 10^8 M_\odot \text{Mpc}^{-3}$, corresponding to a density parameter $\Omega_* = 0.004$ (Salucci & Persic 1999; Cole et al. 2001; Bell et al. 2003; Perez-Gonzalez et al. 2008). Hence, the universal star formation efficiency is only 10%. Several processes could reduce the global star formation rates (SFRs) in galaxies, such as gas heating (McKee & Ostriker 1977; Barkana & Loeb 2000; Efstathiou 2000; Barkana & Loeb 2006; Davé et al. 2006; Muñoz & Loeb 2011; Hopkins et al. 2012), gas stripping (Kawata & Mulchaey 2008; Bekki 2009; Benítez-Llambay et al. 2013), and gas evaporation (Tassis et al. 2003; Wyithe & Loeb 2006; Wyithe & Cen 2007; Pieri & Martel 2007; Yoshida et al. 2007; Duffy et al. 2014; Gnedin & Kaurov 2014), but by limiting the amount of gas available to form stars, galactic outflows are probably the most important feedback mechanism in isolated galaxies (Veilleux et al. 2005; Dalla Vecchia & Schaye 2008; Bower et al. 2012; Falceta-Gonçalves 2013; Puchwein & Springel 2013).

Galaxies of different masses are not equally inefficient in forming stars. The stellar-mass/halo-mass ratio, M_*/M_h ,

peaks at a halo mass $M_h = 10^{12} M_\odot$, with a ratio $M_*/M_h \sim 0.03$ (Behroozi et al. 2010; Moster et al. 2010). At both lower and higher masses, the ratio decreases, suggesting that two different processes might be involved. Feedback by supernovae can power galactic winds in low-mass galaxies (Benson et al. 2003; Mo et al. 2004; Puchwein & Springel 2013; Mayika et al. 2014; McNaught-Roberts et al. 2014), but this process is inefficient at high masses. As the total galaxy mass increases, the binding energy of the gas increases faster than the energy released collectively by supernovae (Pieri et al. 2007; Germain et al. 2009). Therefore, an alternate source of energy, such as AGN feedback, is needed to explain galactic winds in high-mass galaxies (Benson et al. 2003; Kawata & Gibson 2005; Bower et al. 2006; Somerville et al. 2008; Guo et al. 2011; Bower et al. 2012).

This basic *negative feedback scenario* can explain the observed galactic outflows, the observed M_*/M_h ratios in high-mass galaxies, and possibly the observed relations between SBH mass, velocity dispersion, and bulge stellar mass. However, it relies on an efficient coupling between the energy released by the AGN and the ISM gas. The energy deposited by the AGN can either increase the gas temperature (thermal feedback), or accelerate the gas to large velocities (kinetic feedback). Thermal feedback is less efficient than kinetic feedback, because a fraction of the thermal energy will be radiated away before the resulting pressure gradients can accelerate the gas. The relative importance of thermal vs. kinetic feedback is still debated (e.g. Barai et al. 2014). Also, it has been suggested that in an inhomogeneous ISM, AGN outflows will follow the path of least resistance, forming elongated cavities instead of spherical ones (Germain et al. 2009; Cresci et al. 2015). In this case, a substantial amount of gas might remain inside the host galaxy, and increasing the AGN luminosity will not increase the fraction of gas being ejected, but rather the velocity of the gas that is ejected. If the gas is not entirely expelled from the galaxy, the fraction of gas that remains in the galaxy could then be affected *positively* by the AGN feedback. The injection of energy and momentum into the surrounding gas can generate shock waves that will trigger star formation by compressing the gas into dense shells (Ishibashi & Fabian 2012; Cresci et al. 2015).

Observations reveal the existence of two AGN accretions modes, a radiatively efficient mode associated with low-mass central black holes and high SFRs that would result from interactions and mergers (Kauffmann et al. 2003; Best et al. 2005; Johansson et al. 2009; Kauffmann & Heckman 2009; Smolcic 2009; Best & Heckman 2012; Capelo et al. 2015), and a radiatively inefficient accretion mode associated with high-mass central black holes and low SFRs that would result from secular evolution (Best et al. 2005, 2006; Allen et al. 2006; Hardcastle et al. 2006, 2007; Gaspari et al. 2013). In both cases, the anti-correlation between black hole mass and SFR is consistent with negative feedback. Ellison et al. (2015b) showed that the SFRs of AGN hosts depend critically on the selection criteria, with radio-selected AGN having very low SFRs, optically-selected AGN having marginally suppressed SFRs, and mid-IR-selected AGN having elevated SFRs.

Several recent observational and numerical studies suggest that both positive and negative feedback are present in AGN hosts, though their relative importance is unclear.

Balmaverde et al. (2016) considered a sample of 132 low-redshifts quasars ($z < 1$) selected from the Sloan Digital Sky Survey, with corresponding photometric data from *Herschel*. They divided their sample into strong-outflow and weak-outflow galaxies, and found no evidence of the SFR being lower in galaxies with stronger outflows, as the negative feedback scenario would predict. To the contrary, the SFRs are comparable to or even higher than the ones in weak-outflow galaxies. Cresci et al. (2015) studied a radio-quiet QSO at redshift $z = 1.59$ using SINFONI NIR integral field spectroscopy. Their study reveals the presence of a powerful, highly-anisotropic outflow that expels gas from the host galaxy along a cavity surrounded by a compressed layer of gas. Star formation is suppressed inside the cavity, while enhanced in the surrounding layer. Carniani et al. (2016) studied two QSOs at high redshift ($z \sim 2.5$) that exhibit very strong outflows, and found that the effect on star formation was marginal, and affected only a small region within the host galaxy. These authors point out that their results are consistent with the positive + negative feedback model suggested by Cresci et al. (2015). Roos et al. (2015) performed a numerical simulation of the evolution of a massive galaxy hosting an AGN. Their simulation produces a significant outflow, but the SFR is reduced by only a few percent, because star-forming clouds are too dense to be affected significantly by AGN feedback. These authors conclude that the effect of AGN feedback on the SFR of high-redshift galaxies is marginal. In a very recent zoom-in simulation of a barred galaxy in a cosmological context, Spinoso et al. (2017) found that in the presence of AGN feedback, most of the gas in the centre of the galaxy is promptly consumed by star formation, while only a small fraction is accreted by the central black hole.

While AGN feedback can greatly affect the evolution of the host galaxy, the structure and dynamical evolution of the galaxy will, in turn, influence the growth of the AGN. In order to produce a luminous AGN, a galaxy requires a ready source of gas, which may be reduced by star formation and galactic outflows. Also, the galaxy must have the ability to drive this gas toward the centre. This latter effect is particularly important in barred galaxies. In the presence of a bar, gas loses angular momentum and falls toward the centre of the galaxy, where it tends to form an elongated orbit inside the stellar bar (Athanasoula 1992; Combes & Elmegreen 1993; Maciejewski et al. 2002; Martel et al. 2013, hereafter Paper I). If the gas eventually reaches the centre of the galaxy, it might accrete onto the central black hole and fuel the AGN (Shlosman et al. 1989; Shlosman & Noguchi 1993; Heller & Shlosman 1994; Combes 2003; Jogee 2006). Several observational studies find a higher bar fraction in AGN-host galaxies than non-AGN ones (Arsenault 1989; Knappen et al. 2000; Laine et al. 2002; Galloway et al. 2015). However, other studies do not find any significant difference (Moles et al. 1995; McLoed & Rieke 1995; Mulchaey & Regan 1997; Ho et al. 1997; Laurikainen et al. 2004; Hao et al. 2009; Bang & Ann 2009; Lee et al. 2012; Cheung et al. 2014), or find a difference mostly in blue galaxies (Oh et al. 2012). Whilst changes in metallicity and SFRs are widely supported by observations, the link between bars and AGN fueling has remained contentious. Several observations reveal enhanced star formation in the central regions of barred galaxies

(Ho et al. 1997; Martinet & Friedli 1997; Hunt & Malkan 1999; Emsellem et al. 2001; Knapen et al. 2002; Jogee et al. 2005; Ellison et al. 2011). Gas converted into stars can no longer be accreted onto the central black hole, and the relative importance of these two competing processes is an unresolved issue (Oh et al. 2012; Alonso et al. 2014; Cisternas et al. 2015).

Despite conflicting observational results, in simulations, bars represent a very effective way to move gas to the nuclear regions and hence trigger an AGN. Therefore, simulations of barred galaxies represent an excellent laboratory for the study of AGN feedback in galaxies. We have performed a series of 10 chemodynamical simulations of isolated barred galaxies, and for comparison, two simulations of isolated unbarred galaxies, with various prescriptions for AGN feedback. Our goal is to determine the effect of AGN accretion and feedback on the star formation history of barred spiral galaxies. In particular, we want to determine if the AGN will deplete the gas reservoir and quench star formation, or if the feedback effects of the AGN will enhance star formation, and determine what is the timescale of those events, compared to a galaxy of the same mass but with no AGN in its centre.

The remainder of this paper is as follows: in Section 2, we describe our numerical algorithm, including our treatment of AGN feedback. In Section 3, we present our suite of simulations. Results are presented in Section 4 and discussed in Section 5. Summary and conclusions are presented in Section 6.

2 THE NUMERICAL METHOD

2.1 The GCD+ Algorithm

All the simulations in this paper were performed using the numerical algorithm GCD+ (Kawata & Gibson 2003; Rahimi & Kawata 2012; Barnes et al. 2012; Kawata et al. 2013, 2014). GCD+ is a three-dimensional tree/smoothed particle hydrodynamics (SPH) algorithm which simulates galactic chemodynamical evolution, accounting for hydrodynamics, self-gravitation, star formation, supernova feedback, metal enrichment and diffusion, and radiative cooling. Star formation is handled by transforming gas particles into star particles: if the local velocity of the gas particles is convergent and one of them exceeds a given density threshold n_{th} , the gas particle may transform into a star particle with a probability weighted by its density. The star particles have their mass distributed accordingly to the Salpeter (1955) initial mass function, and the metal enrichment they produce from Type II and Ia supernovae is tabulated from Woosley & Weaver (1995) and Iwamoto et al. (1999).

Four main parameters govern the star formation rate and the supernovae feedback (Rahimi & Kawata 2012) and are fixed as follows: the supernova energy output $E_{\text{SN}} = 1 \times 10^{50} \text{ erg}$, the stellar wind energy output $E_{\text{SW}} = 5.0 \times 10^{36} \text{ erg s}^{-1}$, the star formation efficiency $C_* = 0.02$, and the star formation density threshold $n_{\text{th}} = 1 \text{ cm}^{-3}$.

Cooling rates under the influence of a cosmological UV background are calculated with the CLOUDY spectral synthesis code (Ferland et al. 1998) with the assumption that gas is optically thin, and are tabulated by redshift, density, and temperature for use in the GCD+ code. For the

simulations presented in this paper, we use the tables corresponding to redshift $z = 0$. Cooling is permitted down to 30K. The gravitational softening length is fixed at 90 pc. Gas particles have individual smoothing lengths, which are calculated through an iterative procedure so that each gas particle has ≈ 58 neighbours. However, we impose a minimum smoothing length of 90 pc. The smoothing length of the particle representing the central black hole is adjusted such that the black hole has ≈ 70 particles within its zone of influence.

2.2 AGN Feedback & Dynamics

Comparative studies of AGN feedback algorithms in major merger simulations (Wurster & Thacker 2013a; Thacker et al. 2014) demonstrate that AGN feedback algorithms greatly differ in their accretion rates, and in the strength and effects of their feedback. These models are generally based on the Bondi accretion rate (Hoyle & Lyttleton 1939; Bondi & Hoyle 1944; Bondi 1952) for accretion onto a dense object,

$$\dot{M}_{\text{Bondi}} = \frac{2\pi G^2 M_{\text{BH}}^2 \rho_{\infty}}{(c_{\infty}^2 + v^2)^{3/2}}, \quad (1)$$

where M_{BH} is the mass of the black hole, ρ_{∞} and c_{∞} are the density and sound-speed of the gas at infinity, respectively, and v is the speed of the black hole relative to this distant gas. Our algorithm is based on the ‘WT’ model of Wurster & Thacker (2013a)

The mass of the black hole is represented by two values: the dynamical mass of the black hole particle (M_{dyn}), and the internal “sub-grid-scale” mass of the physical black hole (M_{SGS}). The sub-grid-scale mass is used to calculate the accretion rate in equation (1) and equation (2) below, while the dynamical mass is used in kinematic interactions with other particles, and in determining the particle’s motion. GCD+ requires that gas and star particles have a constant mass, and so to maintain mass conservation, the dynamical mass increases discretely when an entire particle is accreted, while the sub-grid-scale mass increases continually, as detailed below.

In numerical simulations, the mass of star particles can be a large enough fraction of the black hole particle’s mass that two-body scattering can become significant. To reduce this source of error, we apply a damping force to the black hole particle with a somewhat arbitrary time-scale of 1 Myr. Specifically, every time-step we apply the transform $\mathbf{v}_{\text{BH}} \rightarrow \mathbf{v}_{\text{BH}} \exp[-\Delta t_{\text{BH}}/(1 \text{ Myr})]$, where \mathbf{v}_{BH} is the black hole particle’s velocity vector, and Δt_{BH} is its time-step. This allows the black hole to sink to the minimum of the potential well without being sensitive to two-body kicks. We also force the black hole particle to have a time-step equal to the smallest time-step in the galaxy, or $5 \times 10^4 \text{ yr}$, whichever is smallest. Finally, in some sets of initial conditions (Runs G and I below), we place the black hole at a point (1 pc, 1 pc, 1 pc) from the centre of mass of the galaxy, so that it is not too close to another particle. The black hole particle then quickly finds the minimum of the potential well.

The Bondi accretion rate given by equation (1) uses values at infinity. As is typical in SPH simulations, we replace ρ_{∞} and c_{∞} by the values calculated using the par-

ticles inside the black hole’s smoothing length, and we replace v by the speed of the black hole particle relative to the SPH-smoothed gas velocity at its location. Finally, we use for M_{BH} the internal mass of the black hole M_{SGS} . The smoothing length of the black hole is variable, as with the gas particles, calibrated so that the black hole particle would have ~ 92 neighbouring gas particles if the gas was uniformly distributed. In practice, the flat geometry of the gas near the black hole particle causes the black hole particle to have ~ 70 neighbour particles, still a little above the median number of neighbours for a gas particle. This larger number of neighbours reduces rapid variations in the black hole’s accretion rate.

The maximum accretion rate in spherically symmetric hydrodynamic equilibrium is the Eddington accretion rate,

$$\dot{M}_{\text{Edd}} = \frac{4\pi GM_{\text{BH}}m_p}{\epsilon_r \sigma_T c}, \quad (2)$$

where m_p is the mass of a proton, ϵ_r is the radiative efficiency, and σ_T is the Thomson cross-section. The radiative efficiency is a free parameter, which we set to $\epsilon_r = 0.1$, following Shakura & Sunyaev (1973). We also increase our numerical accretion rate by a factor α , to reflect the underestimation of sound-speeds that results from resolution limits (Booth & Schaye 2009). Hence our numerical accretion rate is

$$\dot{M}_{\text{num}} = \min(\dot{M}_{\text{Edd}}, \alpha \dot{M}_{\text{Bondi}}). \quad (3)$$

We select $\alpha = 100$, following Springel et al. (2005).

During each timestep Δt , the accretion rate \dot{M}_{num} is calculated using equations (1)–(3) with $M_{\text{BH}} = M_{\text{SGS}}$. Then the internal mass is augmented using $M_{\text{SGS}} \rightarrow M_{\text{SGS}} + \Delta M$, where $\Delta M = \dot{M}_{\text{num}} \Delta t$, to account for mass being accreted onto the black hole. However, the dynamical mass M_{dyn} , which enters into the calculation of gravity, is left unchanged, and the mass of neighbouring particles is also left unchanged. To ensure approximate agreement between the dynamical mass and the internal mass of the black hole particle, a gas particle is accreted onto the black hole particle when the internal mass exceeds the dynamical mass by half of the mass of a gas particle. This closest gas particle to the black hole particle is deleted, and its mass is added to the dynamical mass of the black hole particle. This insures that M_{dyn} always remains within one half of a gas particle mass of M_{SGS} during the course of the simulation.¹

A fraction $\epsilon_r = 0.1$ of the accreted rest-mass energy $\Delta M c^2$ is returned in the form of feedback. As the ISM is largely optically thin, only a portion of this energy ($\epsilon_c = 0.05$) is coupled to the ISM, giving a feedback energy of

$$\Delta E = \epsilon_r \epsilon_c \Delta M c^2. \quad (4)$$

This energy is divided evenly amongst all particles within the black hole particle’s smoothing length. A fraction, f_{th} of the energy is applied as thermal energy, with the remaining applied directly as kinetic energy by applying a radially directed momentum kick of $p = (1 - f_{\text{th}})c\Delta E/N_f$ to all N_f particles within the black hole particle’s smoothing length.

¹ We note that the particles being accreted are typically located at a distance from the black hole comparable to or only slightly larger than the gravitational softening length.

Barai et al. (2014) compared thermal feedback with direct input of kinetic energy, and found that kinetic feedback has a stronger effect, producing a clear outflow.

3 THE SIMULATIONS

3.1 Initial Conditions

For generating the initial conditions of our simulations, we use the same technique as in Grand et al. (2015) and Carles et al. (2016) (hereafter Paper II). Since our goal is to assess the importance of positive and negative feedback on star formation, we examine galaxies where AGN feedback is strong, but not so strong as to remove the gas from the galaxy and completely shut off star formation. The shape of the M_h/M_* relation shows that SNe feedback dominates for masses $M_* < 3 \times 10^{10} M_\odot$, whereas most of the gas in blown out for much larger masses (Behroozi et al. 2010; Moster et al. 2010). For this reason, we selected an initial stellar mass $M_* = 5.80 \times 10^{10} M_\odot$, which is near the bottom of the “AGN regime.” The corresponding halo mass is $M_{200} = 2.306 \times 10^{12} M_\odot$.

We set up the stellar disc using an exponential surface density profile:

$$\rho_* = \frac{M_*}{4\pi z_* R_*^2} \text{sech}^2\left(\frac{z}{z_*}\right) e^{-R/R_*}, \quad (5)$$

where R_* is the scale length, z_* is the scale height, and R and z are the radial and horizontal coordinates respectively. The gaseous disc has the same radial exponential surface density, but its height is determined by imposing an initial hydrostatic equilibrium within the gaseous disc (Springel et al. 2005). We then set an initial radial metallicity profile in both the stellar and gaseous populations, with the iron abundance being given by

$$[\text{Fe}/\text{H}] = 0.2 - 0.05R, \quad (6)$$

where R is in kpc. α -elements are initially only present in the stellar component and their abundance is given by

$$[\alpha/\text{Fe}] = -0.16[\text{Fe}/\text{H}](R). \quad (7)$$

We add to this value a gaussian scatter of 0.02 dex to create a local dispersion of the abundances. The star particles are assigned an initial age using an age-metallicity relation $[\text{Fe}/\text{H}] = -0.04 \times \text{age}(\text{Gyr})$. We do not use particles to represent the dark matter. Instead, we assume a static halo with an NFW profile (Navarro et al. 1996), an approximation which is appropriate for simulations of isolated galaxies. This dark matter halo is characterized by a mass M_{200} and a concentration parameter c . We use two different values of c : 8 and 20. As shown in Papers I and II, the lower value allows the formation of a bar by instability, while the larger value suppresses it.

The scale length of the stellar disc is calculated using the relation between R_{50} , the half-light radius, and M_* , the mass of the stellar disc, as found by Shen et al. (2003):

$$R_{50}(\text{kpc}) = \gamma M_*^\alpha \left(1 + \frac{M_*}{M_0}\right)^{\beta-\alpha}, \quad (8)$$

where γ is a scaling factor, M_0 is the characteristic mass of the transition between the low-mass behaviour as M_*^α and the high-mass one as M_*^β . Continuing to follow Shen et al.

Table 1. Parameters of the simulations.

Run	barred	N_{gas}^a	N_{star}^b	f_{gas}^c	t_{AGN}^d	f_{kin}^e
A	yes	122694	514541	0.192
B	yes	122694	514541	0.192	0	0
C	yes	122694	514541	0.192	0	0.1
D	yes	122694	514541	0.192	0	0.2
E	yes	122694	514541	0.192	0.5	0.1
F	yes	122694	514541	0.192	0.5	0.2
G	yes	61347	575888	0.096
H	yes	61347	575888	0.096	0	0.2
I	yes	30674	606561	0.048
J	yes	30674	606561	0.048	0	0.2
K	no	122694	514541	0.192
L	no	122694	514541	0.192	0	0.2

^a Initial number of gas particles.

^b Initial number of star particles.

^c Initial gas fraction. Galaxies with $f_{\text{gas}} = 0.192, 0.096,$ and 0.048 are “gas-normal,” “gas-poor,” and “gas-very-poor,” respectively.

^d Time in Gyr when AGN accretion and feedback is turned on.

^e Fraction of feedback energy applied as kinetic energy.

(2003), we use $\gamma = 0.1$, $M_0 = 3.98 \times 10^{10} M_{\odot}$, $\alpha = 0.14$, and $\beta = 0.39$ to evaluate the half-light radius for a given mass. Assuming that the half-light radius corresponds roughly with the half-mass radius, we integrate the density profile of the stellar disc (eq. 5) up to R_{50} to obtain a transcendental relation between R_* and R_{50} which lets us compute the scale length from the disc mass. For the mass considered in this paper, this gives a scale length $R_* = 2.4$ kpc. We also set the scale height of the stellar disc to $z_* = 0.48$ kpc.

We set the fiducial parameters for the gaseous disc using the same relation as Cox et al. (2006), itself derived from Bell et al. (2003):

$$\log M_{\text{gas}} = 0.78 \log M_* - 1.74, \quad (9)$$

where both masses are expressed in units of $10^{10} M_{\odot}$. This gives a gas mass $M_{\text{gas}} = 1.38 \times 10^{10} M_{\odot}$, and an initial gas fraction $f_{\text{gas}} = M_{\text{gas}} / (M_* + M_{\text{gas}}) = 0.192$. We will actually experiment with various values of f_{gas} , while keeping $M_* + M_{\text{gas}}$ constant. The scale length of the gas disc is $R_{\text{gas}} = 4.79$ kpc. To determine the vertical distribution of the gas, we follow the prescription described in Springel et al. (2005). We first use CLOUDY to determine an effective equation of state of the form $P = P(\rho)$. The initial vertical distribution of the gas disc is then set so that it is in hydrodynamic equilibrium. This produces a flared disc with a scale height z_{gas} of 30 pc at the centre and 600 pc at $R = 40$ kpc.

Finally, we put the black hole initially at rest at the centre of mass of the galaxy, and initialise its masses at $M_{\text{dyn},i} = M_{\text{SGS},i} = 10^6 M_{\odot}$. The black hole particle is included even in simulations without AGN feedback, to prevent the small dynamical effects of the presence of a black hole particle from influencing the results.

3.2 Runs and Parameters

We performed a series of 12 simulations. Run A is a simulation of a barred galaxy without an AGN. In Runs B, C, and D, we include an AGN, and vary the relative strength of thermal and kinetic feedback.

In all simulations, we start with an axisymmetric disc, and the bar forms by instability. However, there are other processes that can lead to the formation of a bar. To investigate the possibility that the AGN turns on in a galaxy where the bar is already formed, we have performed two simulations, E and F, where we delay the turn-on of AGN feedback until the bar has formed, at $t_{\text{AGN}} = 0.5$ Gyr.

Runs A–F all have an initial gas fraction $f_{\text{gas}} = 0.192$, consistent with equation (9). Runs G and I, are similar to Run A (no AGN), and Runs H and J are similar to Run D (same AGN feedback prescription), but these runs start with a lower initial gas fraction. Runs K and L are similar to Runs A and D, respectively, but we used a concentration parameter $c = 20$ to prevent the formation of a bar. The parameters of the simulations are listed in Table 1. N_{gas} and N_{star} are the initial number of gas and star particles respectively. f_{gas} is the initial gas fraction, t_{AGN} is the time when AGN accretion and feedback is turned on, and $f_{\text{kin}} = 1 - f_{\text{th}}$ is the fraction of feedback energy applied as kinetic energy. With these parameters, each particle has a mass of $8.60 \times 10^4 M_{\odot}$. We will refer to galaxies K, L, and A through F as “gas-normal,” galaxies G and H as “gas-poor,” and galaxies I and J as “gas-very-poor.”

4 RESULTS

4.1 Bar Formation

Figures 1 and 2 show the column density of gas (left panels) and stars (right panels) at $t = 400$ Myr, for Runs A, D, and K. Figure 1 shows the entire galaxies, while Figure 2 shows zoom-ins of the central regions. Runs A and D differ by the presence of an AGN. In both runs, we clearly see the bar and the pattern of spiral arms, both in the gas and stars. However, at that particular time the bar in Run D is significantly longer and more prominent than in Run A, because it forms earlier. Runs A and K differ by the presence of a bar. The spiral pattern can be seen in the gas for Run K, but it is much less prominent than in the runs with a bar. Not having a bar greatly reduces the gas flow toward the centre of the galaxy, resulting in a much flatter surface density gradient and a much lower central surface density, both in stars and gas. Results for Run L are similar. The numerous cavities we see in the gas distributions are caused by SNe feedback.

As in Paper II, we calculate bar strength using a method proposed by Athanassoula & Misiriotis (2002), based on the components of the Fourier decomposition of the azimuthal distribution of particles. In Figure 3 we present the evolution of the bar strength as a function of time for gas-normal galaxies. In the absence of AGN feedback (Run A, black line), the bar strength increases steadily, reaching a peak value of $A_2 = 0.34$ by $t = 500$ Myr. Afterward, the value of A_2 strongly oscillates, with a net decrease over time, down to $A_2 \sim 0.2$ at $t = 1.5$ Gyr. With AGN feedback included (Runs B, C, and D), the bar grows faster and the peak value of A_2 is reached earlier, after which the evolution is similar to Run A. In all simulations, the initial disc is in a state of unstable equilibrium. AGN feedback seems to hasten the growth of the instability, possibly by perturbing the equilibrium earlier. A similar effect was noticed by Spinoso et al. (2017). Even though Run C is an intermediate between Runs B and

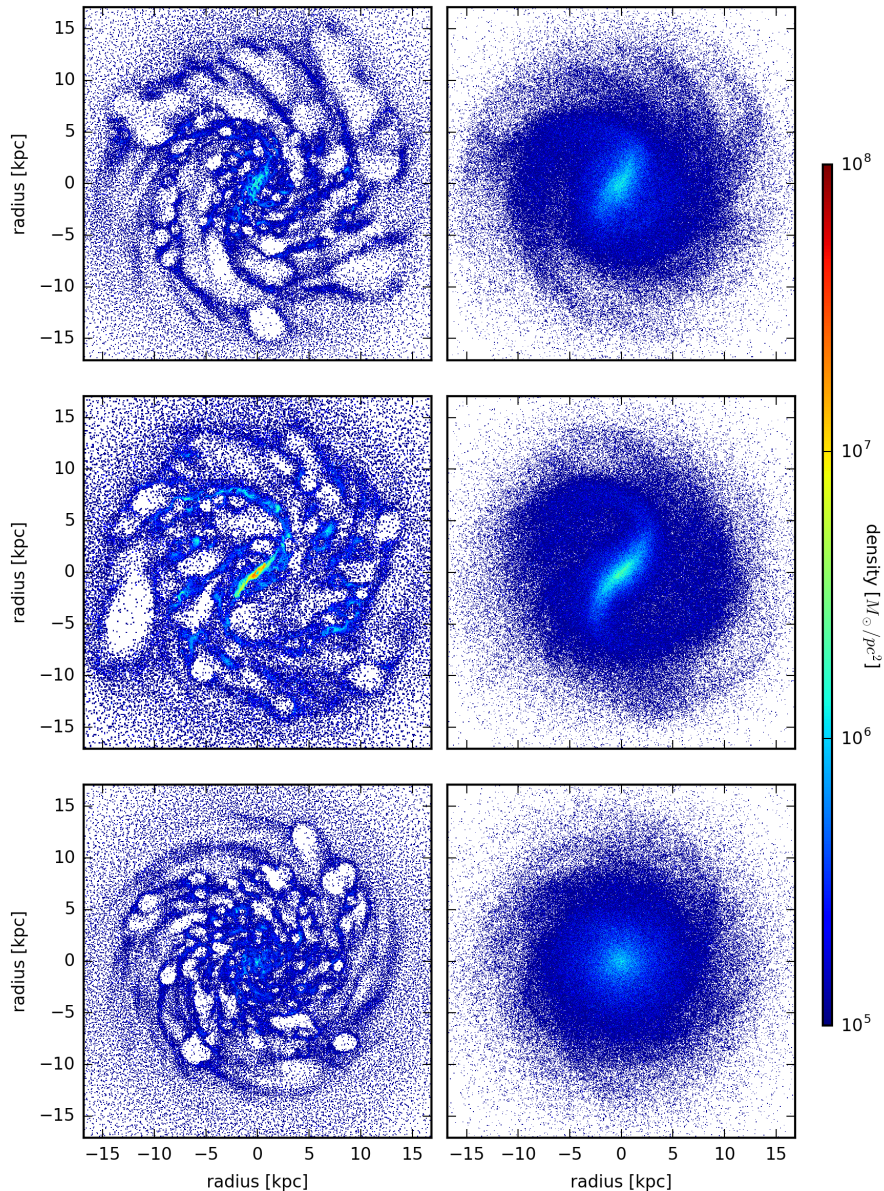


Figure 1. Configuration of the system at $t = 400$ Myr, showing the column densities of gas (left) and stars (right). Top row: Run A (bar, no AGN); middle row: Run D (bar + AGN); bottom row: Run K (no AGN, no bar).

D, it has the lowest peak value: $A_2 = 0.30$, compared to 0.36 for Run B and 0.38 for Run D. Such non-monotonicity is not unexpected, considering again that the bar in these simulations forms by instability. In Runs E and F, we turn on AGN accretion and feedback at $t = 500$ Myr, which coincidentally corresponds to the moment when the bar has reached its maximum strength. Adding feedback this late does not significantly affect the subsequent evolution of the bar.

4.2 Central Gas Reservoir

Figure 4 shows the evolution of the gas mass in the central 1 kpc, for gas-normal galaxies.² Comparing the location and height of the peaks in the top panel with the ones in Figure 3, we see that the early evolution of the central gas mass almost perfectly mirrors the early evolution of the bar strength. The bar forms earlier in simulations with AGN feedback, allowing the central gas density to build up more rapidly. Afterward, at $t > 500$ Myr, the mass of gas decreases

² The *centre* of the galaxy is defined as the centre of the NFW dark matter halo. As we explained in § 2.1, the black hole is allowed to move, and can be slightly displaced relative to the centre.

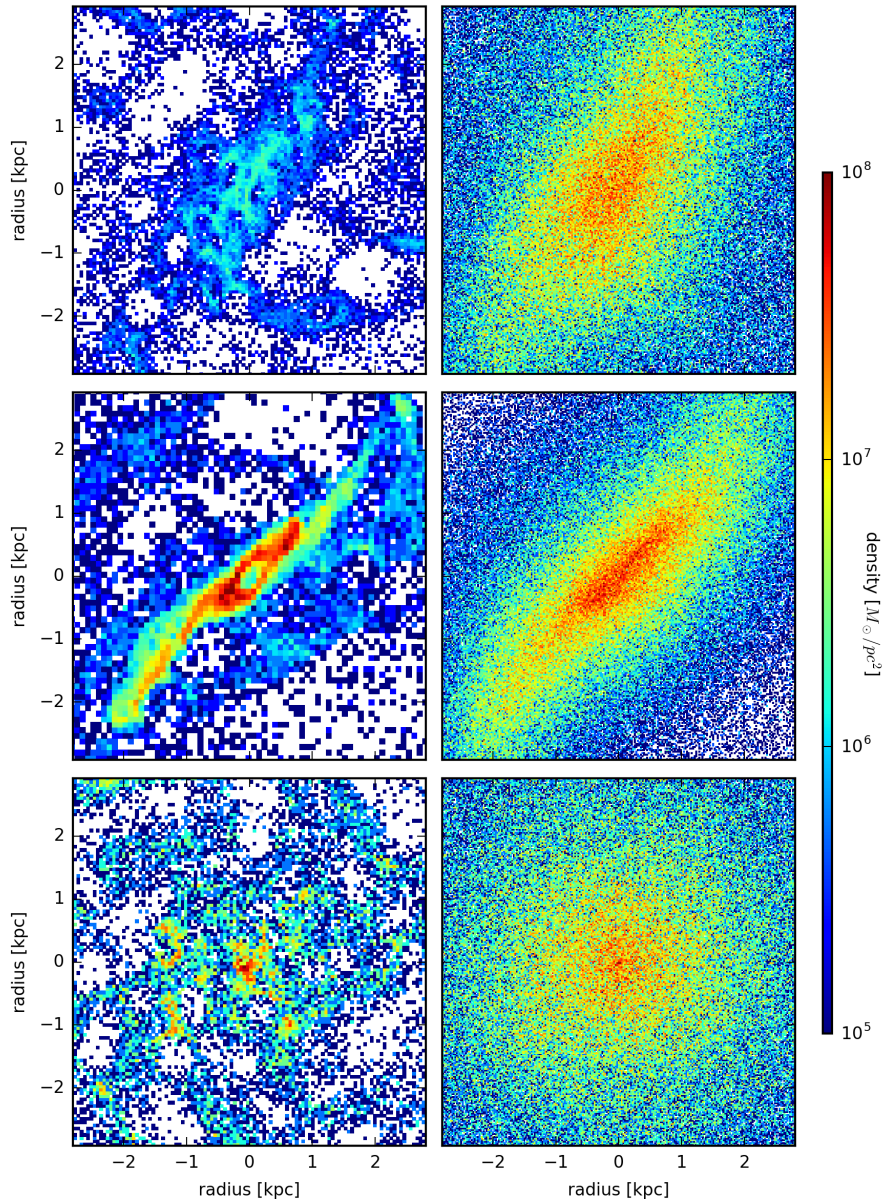


Figure 2. Zoom-in of the regions shown in Fig. 1.

while the bar remains present. After $t = 800$ Myr, the evolution is essentially the same for all runs, indicating that AGN accretion and feedback has little effect in the central 1 kpc once most of the central gas has been either accreted, converted to stars or pushed out to larger radius. In barred galaxies, the central gas mass rapidly peaks because of bar-induced gas inflow, and then drops rapidly. This reduction in central gas mass is caused primarily by gas being converted to stars, as we will show below. The situation is drastically different in unbarred galaxies. Without feedback (Run K, dashed black line), the gas mass in the central 1 kpc region increases slowly and monotonically, with a slight change of slope at $t \sim 900$ Myr. With feedback (Run L, dashed red line), the growth is even slower and also more irregular, but does not have any significant peak.

4.3 Black Hole Growth and Feedback

Figure 5 shows the black hole mass M_{BH} vs. time, for all gas-normal galaxies except Runs A and K, which contain no AGN.³ For the first 300 Myr, the black holes grow at essentially the same rate in Runs B, C, and D. During that period, AGN feedback is too weak to significantly affect the accretion rate onto the black hole. $t = 300$ Myr is about the time when the bar strength reaches $A_2 = 0.2$. As we showed in Section 4.2, a stronger bar drives larger amounts of gas toward the centre, increasing both the accretion rate

³ Unless specified otherwise, the black hole mass M_{BH} refers to the sub-grid mass M_{SGS} , and not the dynamical mass M_{dyn} (see Section 2.2).

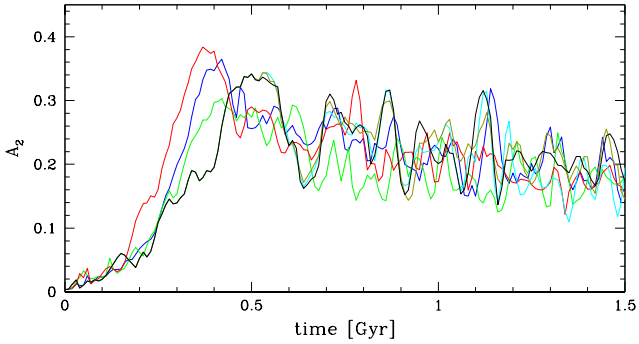


Figure 3. Bar strength vs. time for gas-normal galaxies. Black line: Run A (no AGN); blue line: Run B (thermal feedback); green line: Run C ($f_{\text{kin}} = 0.1$); red line: Run D ($f_{\text{kin}} = 0.2$); cyan line: Run E (delayed AGN, $f_{\text{kin}} = 0.1$); gold line: Run F (delayed AGN, $f_{\text{kin}} = 0.2$). Note that gold and cyan lines are identical to black line at $t < 0.5$ Gyr.

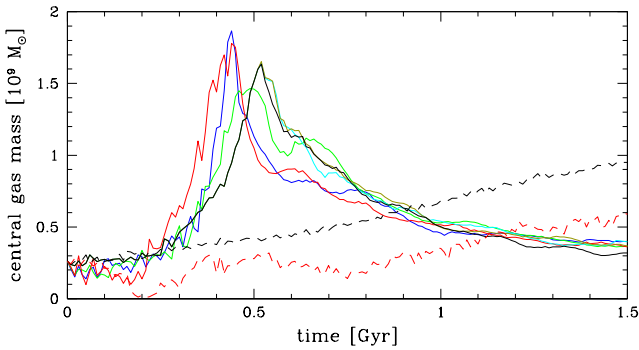


Figure 4. Gas mass in the central region vs. time for gas-normal galaxies. Solid black lines: Run A (No AGN); blue lines: Run B (thermal feedback); green lines: Run C ($f_{\text{kin}} = 0.1$); solid red lines: Run D ($f_{\text{kin}} = 0.2$); cyan lines: Run E (delayed AGN, $f_{\text{kin}} = 0.1$); gold lines: Run F (delayed AGN, $f_{\text{kin}} = 0.2$); dashed black lines: Run K (no bar, no AGN); dashed red lines: Run L (no bar, $f_{\text{kin}} = 0.2$). Note that gold and cyan lines are identical to black line at $t < 0.5$ Gyr.

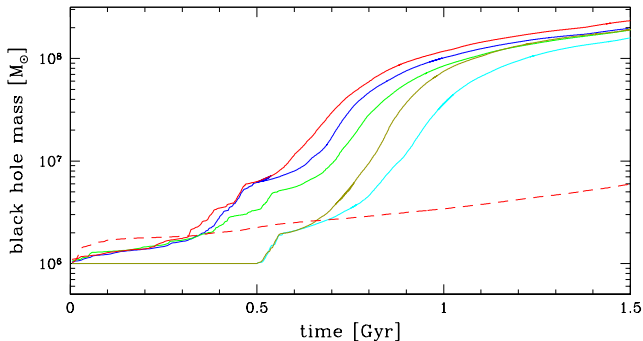


Figure 5. Black hole mass vs. time for gas-normal galaxies. Blue line: Run B (thermal feedback); green line: Run C ($f_{\text{kin}} = 0.1$); solid red line: Run D ($f_{\text{kin}} = 0.2$); cyan line: Run E (delayed AGN, $f_{\text{kin}} = 0.1$); gold line: Run F (delayed AGN, $f_{\text{kin}} = 0.2$); dashed red line: Run L (no bar, $f_{\text{kin}} = 0.2$). Note that gold and cyan lines are identical at $t < 0.5$ Gyr.

and the strength of the feedback. The subsequent evolution differs for Runs B, C, and D. The difference in black hole mass between Runs C and D reaches a factor of 2.5 around $t = 700$ Myr, but by $t = 1.5$ Gyr the differences are less than 50%. We find again a non-monotonicity in the results: Run C, which has the intermediate kinetic feedback ($f_{\text{kin}} = 0.1$), lies below Runs B and D and not between them. The time when the bar forms and drives gas toward the centre appears more critical than the nature of the feedback in determining the growth rate of a black hole.

In Runs E and F, accretion and feedback are turned off until $t = 500$ Myr. Once it is turned on, the black hole mass first grows very rapidly, because a large amount of gas has been accumulated in the centre, waiting to be accreted. Initially, the mass growth is the same in both runs, and the black holes double their masses in less than 50 Myr. They start to differ once feedback becomes important, and from there the evolution is qualitatively similar to Runs B, C, and D. In all five runs, feedback starts to make a difference once the black hole reaches a mass of order $M_{\text{BH}} \sim 2 \times 10^6 M_{\odot}$, that is, double its initial mass. For Runs B, C, and D, this coincides with the time when the bar reaches its maximum strength.

The dashed red line in Figure 5 shows the growth of the black hole mass for Run L. In the absence of bar-driven gas inflow, the black hole mass increases slowly and steadily. By 1 Gyr its mass has increased by a factor of 6, compared to 234 for Run D. Interestingly, there is a sudden increase in mass at the beginning of the simulation for Run L, where the mass of the black hole goes up by 50% after a mere 25 Myr. We also see a weaker initial increase in Runs B, C, and D. In all cases, the black hole first accretes the gas located in its vicinity, and then gas flowing from larger distances. The higher concentration parameter in Run L increases the gas density and the depth of the potential at the centre, driving more cooling and more accretion. Afterward, the accretion rate is reduced in Run L because less gas is being driven toward the centre, and by $t = 300$ Myr, Runs B, C, and D have caught up with it.

Figure 6 shows the evolution of the AGN luminosity for gas-normal galaxies. Remember that only a fraction $\epsilon_r \epsilon_c = 0.005$ of the energy released actually couples to the ISM in the form of feedback. Runs B, C, and D follow a similar pattern. The luminosity steadily increases by a factor of order 300, reaching its peak value $L_{\text{AGN}} \sim 6 \times 10^{12} L_{\odot}$ at $t \sim 750$ Myr. Afterward, L_{AGN} slowly decreases, even though the black hole mass keeps increasing. The removal of the gas in the central region reduces the factor ρ_{∞} in equation (1), and this effect eventually dominates over the increase in M_{BH} . In Runs E and F, AGN accretion and feedback is delayed until $t = 500$ Myr, and this in turn delays the time when the AGN luminosity reaches its peak, around $t = 950$ Myr. Except for that, the overall evolution of L_{AGN} is similar to the ones for Runs B, C, and D. We notice large, sudden fluctuations in L_{AGN} , by factors of 20 or more. These fluctuations take place between $t = 200$ Myr and $t = 500$ Myr in Runs B, C, and D, and soon after AGN turn-on in Runs E and F. This corresponds to a period of rapid black hole growth. During that period, the gas accreting onto the black hole can be quite clumpy, leading to sudden variations in ρ_{∞} in equation (1). When a dense clump of gas falls onto the black hole, M_{BH} can increase

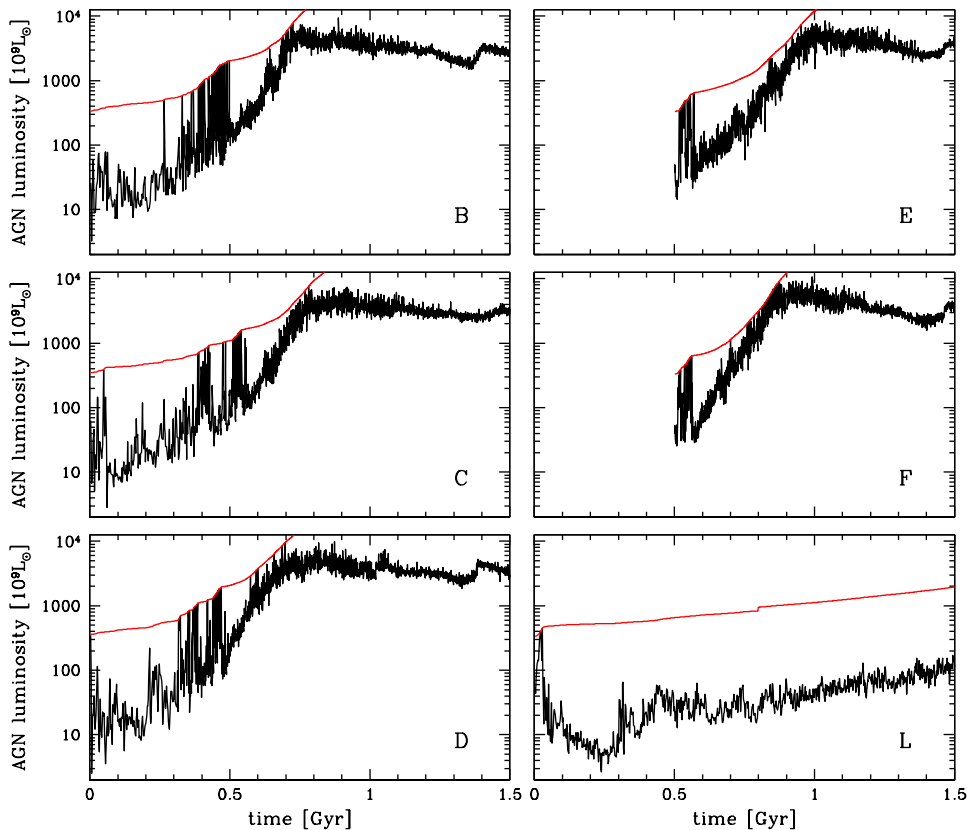


Figure 6. AGN luminosity vs. time for gas-normal galaxies: Run B (thermal feedback), Run C ($f_{\text{kin}} = 0.1$), Run D ($f_{\text{kin}} = 0.2$), Run E (delayed AGN, $f_{\text{kin}} = 0.1$), Run F (delayed AGN, $f_{\text{kin}} = 0.2$), and Run L (no bar, $f_{\text{kin}} = 0.2$). The red lines show the Eddington luminosity.

by a large factor, and the AGN luminosity is then given by the Eddington limit (see eq. 3). This effect becomes less important at later times because the gas is less dense, and a more diffuse gas is less likely to fragment into dense clumps. Notice, however, the peak at $t = 630$ Myr in Run B.

With so little gas in the central region, AGN feedback in unbarred galaxies is greatly reduced. The bottom right panel of Figure 6 shows the AGN luminosity for Run L. After an initial peak caused by the accretion of gas that was located near the black hole in the initial conditions, the luminosity increases slowly. Unlike in barred galaxies, the luminosity never reaches a peak because the accretion rate is too low to exhaust the supply of gas. Throughout the evolution, the luminosity remains consistently an order of magnitude below the Eddington limit, and by $t = 1.5$ Gyr, it is a factor of 30 lower than in Run D.

In Table 2, we compare the final mass of the black hole to the mass of central gas removed during the period of black hole growth. $M_{\text{gas}}^{\text{peak}}$ is the maximum value of the central gas mass, determined from Figure 4, and t_{peak} is the time when this peak value is reached. $M_{\text{gas}}^{\text{final}}$ and M_{BH} are the masses of the central gas and black hole, respectively, at $t = 1.5$ Gyr. $|\Delta M_{\text{gas}}^{\text{final}}| = |M_{\text{gas}}^{\text{final}} - M_{\text{gas}}^{\text{peak}}|$ is the mass of central gas removed. Note that the black hole mass at $t = t_{\text{peak}}$ is negligible compared to the final mass, for all runs. In all cases, $|\Delta M_{\text{gas}}^{\text{final}}|$ exceeds M_{BH} by a factor of five or more, implying that most of the gas removed from the central region

Table 2. Central gas mass and black hole mass

Run	$t_{\text{peak}}[\text{Gyr}]^a$	$M_{\text{gas}}^{\text{peak}}{}^b$	$M_{\text{gas}}^{\text{final}}{}^c$	$ \Delta M_{\text{gas}} {}^d$	$M_{\text{BH}}{}^e$
B	0.44	1.865	0.400	1.465	0.196
C	0.49	1.464	0.368	1.096	0.189
D	0.45	1.752	0.361	1.391	0.189
E	0.45	1.638	0.397	1.241	0.234
F	0.52	1.652	0.368	1.284	0.191

^a Time when the central gas mass reaches its peak value.

^b Central gas mass at $t = t_{\text{peak}}$.

^c Central gas mass at $t = 1.5$ Gyr.

^d Decrease in central gas mass between $t = t_{\text{peak}}$ and $t = 1.5$ Gyr.

^e Central black hole mass at $t = 1.5$ Gyr.

All masses are in units of $10^9[M_{\odot}]$.

is not accreted by the black hole, but instead converted to stars. We note that in Figure 4, the evolution of the central gas mass is essentially the same for Run A, which has no AGN, as in the other runs.

4.4 Star Formation History

We first consider the build-up of the stellar mass in gas-normal galaxies. Figure 7 shows the SFR vs. time for the entire galaxy (top panel) and inside the central 1 kpc region (bottom panel). In the absence of an AGN (Run A,

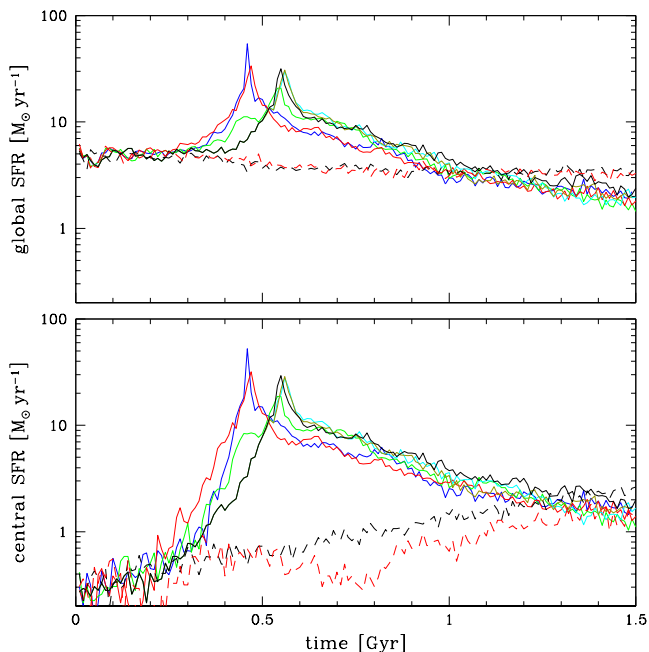


Figure 7. Star formation rate vs. time for gas-normal galaxies. Top panel: entire galaxy; bottom panel: central 1 kpc region. Solid black lines: Run A (No AGN); blue lines: Run B (thermal feedback); green lines: Run C ($f_{\text{kin}} = 0.1$); solid red lines: Run D ($f_{\text{kin}} = 0.2$); cyan lines: Run E (delayed AGN, $f_{\text{kin}} = 0.1$); gold lines: Run F (delayed AGN, $f_{\text{kin}} = 0.2$); dashed black lines: Run K (no bar, no AGN); dashed red lines: Run L (no bar, $f_{\text{kin}} = 0.2$). Note that gold and cyan lines are identical to black line at $t < 0.5$ Gyr.

black line), the global SFR is essentially constant until $t = 400$ Myr, after the bar has formed. Then, star formation rapidly increases, and reaches a peak at $t = 580$ Myr. Afterward, the SFR slowly decreases as the supply of gas available for forming new stars gets depleted. This is fully consistent with the results presented in Papers I and II. The presence of an AGN (Runs B, C, and D) has no significant effect on the SFR until $t = 300$ Myr. The central SFR is small at $t < 300$ Myr, hence most of the stars form in regions that are too far from the centre to be affected by AGN feedback. Also, the accretion rate is still relatively small at this time, as Fig. 6 shows. After $t = 300$ Myr, star formation in the central region becomes important, and the SFR increases faster with simulations with feedback. Looking at Figure 3, we see that $t = 300$ Myr is roughly the time when the bar strength in Runs B and C starts increasing faster than in Run A (the strength of the bar in Run D is already larger at that time). After the peak is reached, the SFR decreases roughly at the same rate as for Run A, and stays about 30% lower than Run A from $t = 800$ Myr until the end of the simulation. Note that at these late stages, star formation occurs almost exclusively in the central region, which explains the similarity of the curves in the top and bottom panels at late times. In all cases, the peak SFR is reached ~ 70 Myr after the peak bar strength is reached. This suggests that the differences in SFR at radii of 1 kpc and larger are mostly a result of the different bar strengths, and that any direct effect of AGN feedback must take place at smaller radii.

Delaying the turn-on of AGN feedback greatly affects the star formation history. In Runs E and F, the AGN is turned on at $t = 500$ Myr, at a time when the bar is formed and star formation in the central regions is well under way. AGN feedback has essentially no effect, because the black hole mass is still at $M_{\text{BH}} = 10^6 M_{\odot}$, resulting in a weak AGN luminosity. It takes another 500 Myr before the AGN luminosity in Runs E and F catches up with Runs C and D, and by that time star formation is well passed its peak. As a result, the time and height of the SFR peaks are essentially the same for Runs A, E, and F, and the late-time evolutions of the SFR are also the same.

The dashed lines in Figure 7 show the SFR for unbarred galaxies. The global SFR slowly decreases with time, dropping by a factor of about 2 after 1.5 Gyr, and is not affected by feedback. The central SFR increases slowly and more irregularly, and the effect of feedback is small except for a brief period around $t = 800$ Myr.

Figure 8 shows “spacetime maps” of the star formation history. Each pixel shows the average SFR in solar masses per year for a particular radial bin over a particular time interval. Looking at Run A, stars initially form at all radii below 9 kpc except at the very centre where the amount of gas available is initially low. As time goes on, angular momentum is redistributed inside the disc. After $t = 500$ Myr, we clearly have two separate regions of active star formation: an inner region ($r < 2$ kpc) where stars are forming inside the bar, and an outer region ($r > 6$ kpc) where stars are forming in the disc, mostly inside the spiral arms. Figure 9 shows a zoom-in of the central 1 kpc region. During the early stages prior to the formation of the bar ($t < 0.4$ Gyr), there is a significant suppression of star formation in the centre at early time, because the gas density is too low to trigger star formation, and gas gets instead accreted by the black hole. In Runs B, C, and D, and also in Run L, the gas that does not get accreted is then pushed to larger radii by the black hole feedback. In Runs A, E, and F, there is no feedback at early time, allowing a limited amount of star formation down to small radii, and the effect is much larger in Run K because the central gas density is initially larger.

At $t > 0.4$ Gyr, the bar has formed in all simulations A through F, and the situation changes drastically. For Run A, we clearly see the peak in star formation at 580 Myr (red area). As time goes on, star formation gets more centrally concentrated. This is consistent with the results of Paper I. The “classic” scenario for the evolution of barred galaxies states that the bar drives gas toward the central region, where it is then converted into stars. We showed in Paper I that stars actually form along the entire length of the bar, and star formation gets more concentrated because the gaseous component of the bar contracts with time.

The effect of AGN feedback on central star formation is clearly visible. Comparing Runs B, C, and D with Run A, we see that in the presence of AGN feedback, the region of active star formation no longer contracts with time, and in Run B it even expands. At $t = 1.5$ Gyr, central star formation is concentrated in the inner 100 pc in Run A, but reaches 400 pc in Runs B, C, and D. The algorithm turns gas particles into star particles when the hydrogen gas density reaches a threshold value $n_{\text{th}} = 1 \text{ cm}^{-3}$. In the absence of AGN feedback, the gas inside the bar reaches that threshold density “on its own,” as the bar contracts with time. In the

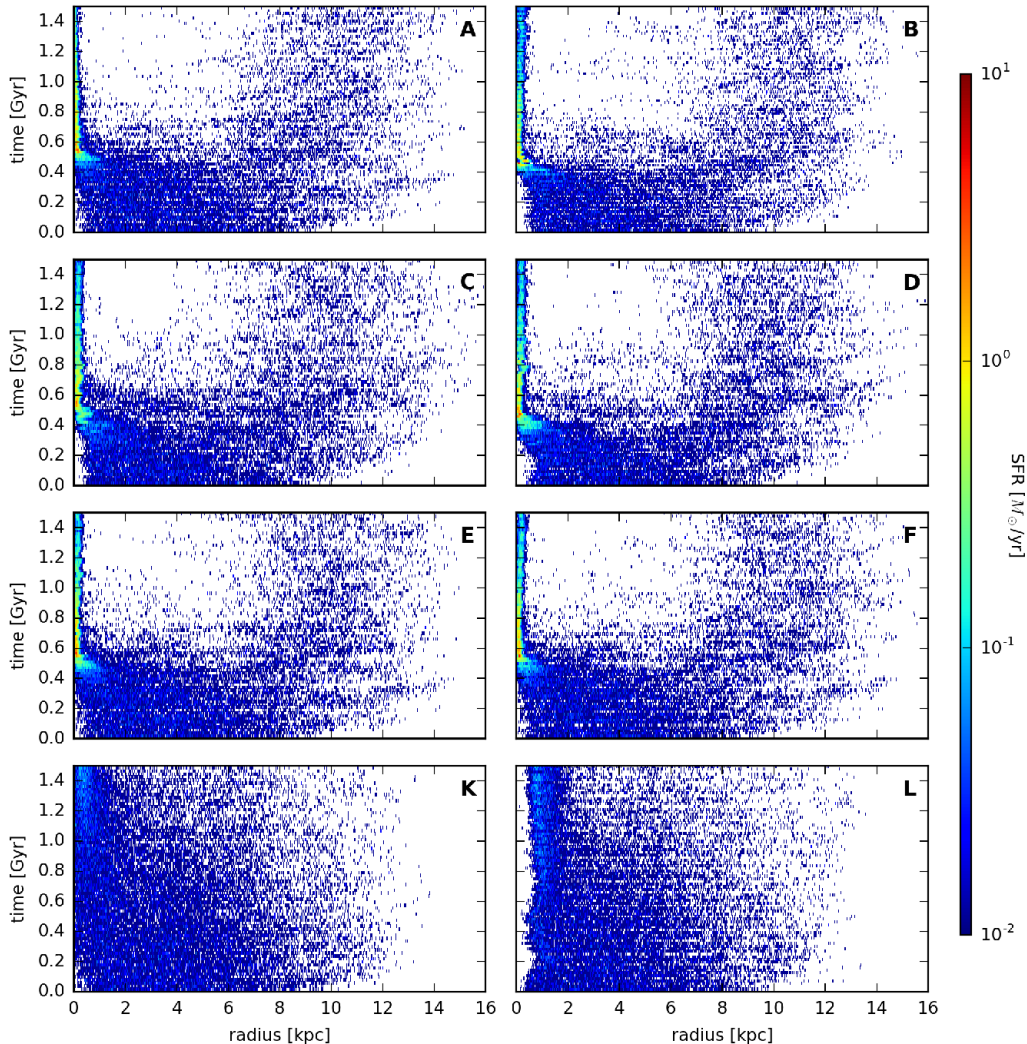


Figure 8. Star formation maps for gas-normal galaxies, showing entire galaxy: Run A (No AGN), Run B (thermal feedback), Run C ($f_{\text{kin}} = 0.1$), Run D ($f_{\text{kin}} = 0.2$), Run E (delayed AGN, $f_{\text{kin}} = 0.1$), Run F (delayed AGN, $f_{\text{kin}} = 0.2$), Run K (no bar, no AGN), and Run L (no bar, $f_{\text{kin}} = 0.2$).

presence of feedback, gas inflowing along the bar toward the centre collides head-on with gas being pushed outward by the AGN, causing a rapid increase in density. This is consistent with the model of Ishibashi & Fabian (2012), where an AGN can trigger star formation by driving a shell of material outward. In our simulations, this results in star formation being pushed to larger radii, starting earlier, and being more violent.

In Runs E and F, feedback is delayed until $t = 0.5$ Gyr. At that time, star formation is well under way. The addition of feedback does not significantly affect the star formation rate, since the gas is already very dense. However, feedback does push the central star formation to larger radii, as it does in Runs B, C, and D.

In Run K, where no bar is present to transfer angular momentum, star formation takes place at all radii up to $r = 12$ kpc. Comparing Runs K and L, we see that feedback pushes central star formation out to larger radii, as it does for barred galaxies. In Run L, star formation is nearly sup-

pressed at radii $r < 0.4$ kpc, and greatly reduced at radii $0.4 < r < 0.8$ kpc. Comparing Runs D and L, we see that the ability to push star formation outward is much higher in the absence of a bar. In Run L, outflowing gas from the AGN is pushing on gas that is nearly standing still, while in Run D it is colliding with gas that is moving inward. Not only it is more difficult to push inflowing gas, but the resulting compression triggers star formation earlier.

In all cases, we find that the effects of AGN feedback are confined to a region much smaller than the “centre,” which we define as the central 1 kpc. This explains why the differences in SFR seen in Figure 7 at early times are mostly due to differences in bar strength.

To further demonstrate that the formation of a star formation “ring” is a result of AGN feedback, and not a dynamical effect, we calculated the rotation velocity profiles, to search for resonances. Figure 10 shows the rotation velocity profiles for Run D, at the initial time and at time $t = 750$ Myr, after the bar is well-formed. Ω , κ , and Ω_p are

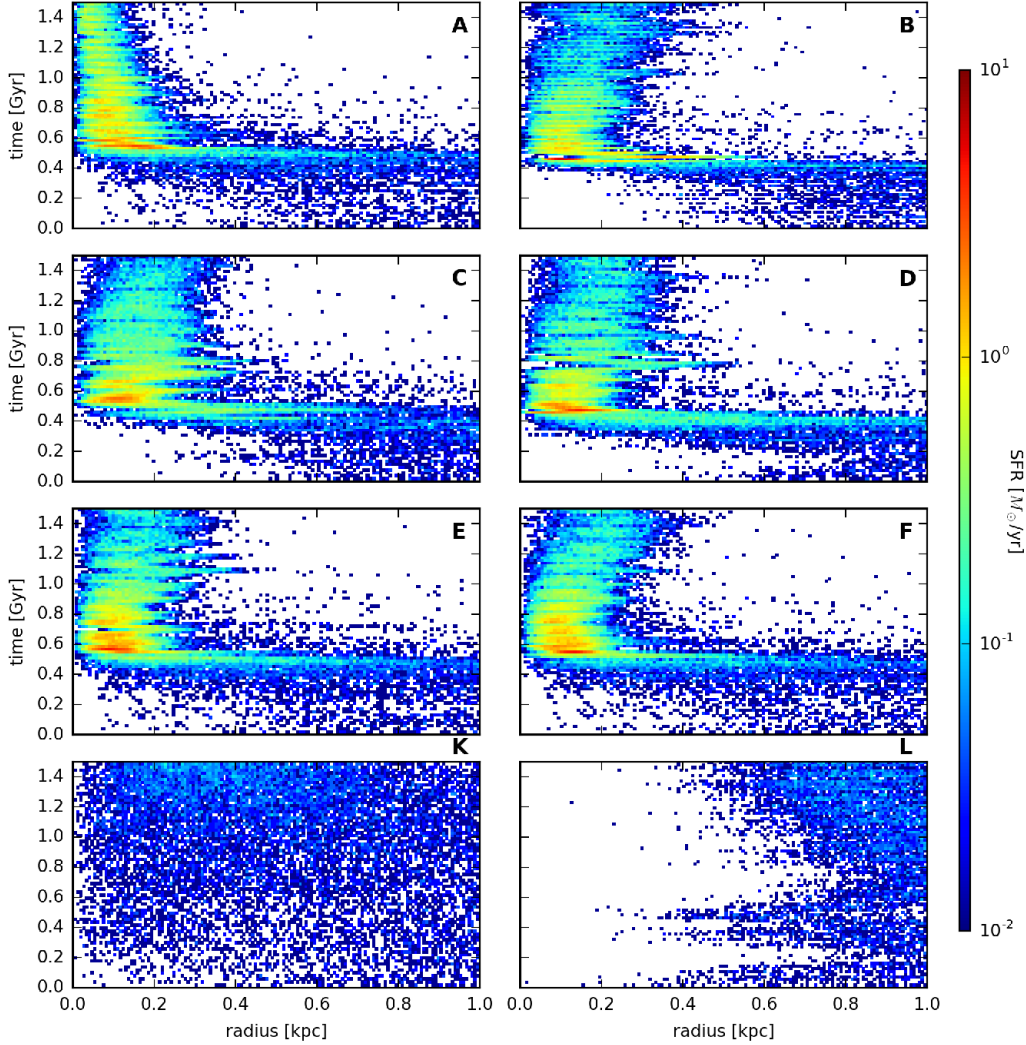


Figure 9. Star formation maps for gas-normal galaxies, showing central 1 kpc region: Run A (No AGN), Run B (thermal feedback), Run C ($f_{\text{kin}} = 0.1$), Run D ($f_{\text{kin}} = 0.2$), Run E (delayed AGN, $f_{\text{kin}} = 0.1$), Run F (delayed AGN, $f_{\text{kin}} = 0.2$), Run K (no bar, no AGN), and Run L (no bar, $f_{\text{kin}} = 0.2$).

the circular frequency, epicycle frequency, and pattern rotation velocity, respectively. At $t = 0$, we find an outer Lindblad resonance at $R = 5.2$ kpc, but no inner Lindblad resonance. This allows the gas to flow toward the centre unimpeded, and accumulate in the central region. At later time, an inner Lindblad resonance appears at radius $R = 0.91$ kpc (solid circle in bottom panel of Fig. 10). Such resonance could lead to the accumulation of gas at that radius, but this does not coincide with the location of the star formation ring. From Figure 9, we estimate that the star formation ring, at $t = 750$ Myr, for Run D, is centred at about $R = 0.14$ kpc (cross in bottom panel of Fig. 10). Therefore, there is no evidence that resonance play any significant role in the formation of a star formation ring.

4.5 Gas Fraction

We now focus on the effect of varying the initial gas fraction in barred galaxies. In Runs A through F (the “gas-normal

galaxies”), the initial gas fraction $f_{\text{gas}} = 0.192$, in accordance with equation (9). Runs G and I, and Runs H and J, are similar to Runs A and D, respectively (same total mass, and for Runs H and J, same AGN feedback prescription as Run D), but in Runs G and H (the “gas-poor” galaxies), the initial gas fraction $f_{\text{gas}} = 0.096$, and in Runs I and J (the “gas-very-poor” galaxies), $f_{\text{gas}} = 0.048$.

The evolution of the bar strength is shown in Figure 11. In this figure and the following ones, we use dotted lines for the runs with no AGN (A, G, I) and solid lines for the runs with AGN (D, H, J). Blue, red, and brown lines show gas-normal, gas-poor, and gas-very-poor galaxies, respectively. When AGN feedback is present there is perhaps a trend of bar formation becoming more delayed with decreasing gas fraction, but this trend is not clear in the runs without AGN feedback, and may not be significant. Once the bar has reached its maximum strength, the subsequent evolution is qualitatively the same for all runs: a strong oscillation superposed on a slow decay. The final values of A_2 are all

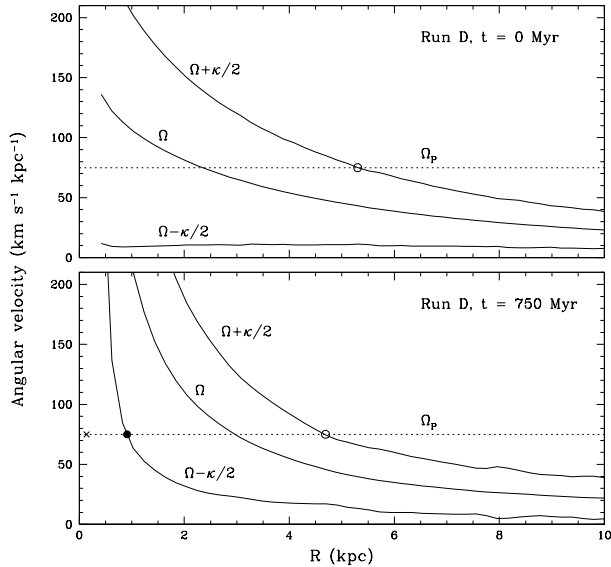


Figure 10. Resonances in the galactic disc, for Run D. Top panel: initial time; bottom panel: at $t = 750$ Myr. Solid lines: $\Omega + \kappa/2$, Ω , and $\Omega - \kappa/2$ versus radius R , as indicated, where Ω is the circular frequency and κ is the epicycle frequency. Dotted lines: pattern rotation velocity Ω_p . The cross, solid circle, and open circles show the location of the star formation ring (inferred from Fig. 9), the inner Lindblad resonance, and the outer Lindblad resonances, respectively.

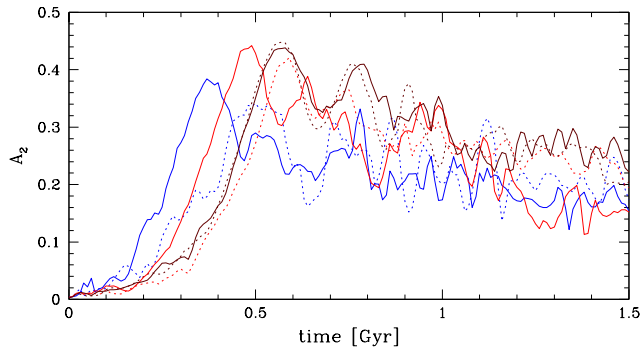


Figure 11. Bar strength vs. time for galaxies with no AGN (dotted lines) and with AGN feedback ($f_{\text{kin}} = 0.2$, solid lines). Blue lines: Runs A and D (gas-normal galaxies); red lines: Runs G and H (gas-poor galaxies); brown lines: Runs I and J (gas-very-poor galaxies).

in the range 0.15–0.25, with no obvious correlation with gas fraction. We notice again a non-monotonicity, with the bar forming slightly earlier for Run I (dotted brown line) than Run G (dotted red line).

Figure 12 shows the evolution of the gas mass in the central 1 kpc, for Runs A, D, and G–J. As the gas fraction is reduced, the central gas mass grows slower, peaks at a lower value, and reaches that peak value later. Gas is a dissipational component that can strengthen instabilities (Elmegreen 2011), and larger gas fractions can help drive gas inwards. Once the peak is passed, the late-time evolution is similar. The amount of gas left in the centre is slightly

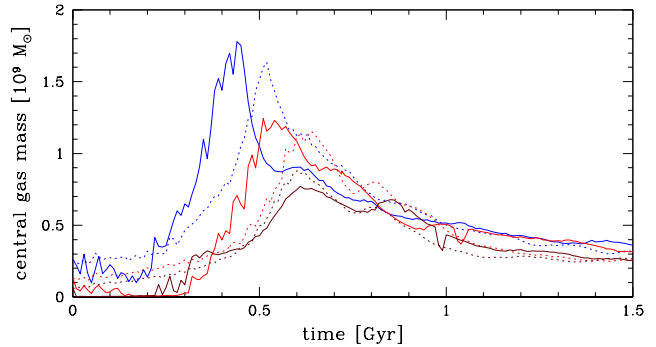


Figure 12. Gas mass in the central region vs. time for galaxies with no AGN (dotted lines) and with AGN feedback ($f_{\text{kin}} = 0.2$, solid lines). Blue lines: Runs A and D (gas-normal galaxies); red lines: Runs G and H (gas-poor galaxies); brown lines: Runs I and J (gas-very-poor galaxies).

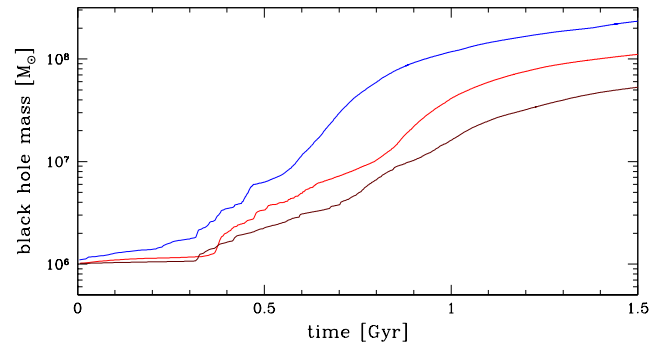


Figure 13. Black hole mass vs. time for galaxies with AGN feedback ($f_{\text{kin}} = 0.2$). Blue line: Run D (gas-normal galaxy); red line: Run H (gas-poor galaxy); brown line: Run J (gas-very-poor galaxy).

reduced when the initial gas fraction is reduced by a factor of 2.

Figure 13 shows the evolution of the black hole mass for Runs D, H, and J. In Run D, the black hole mass starts growing immediately, albeit at a slow rate until $t = 300$ Myr. In Runs H and J, the black hole mass is nearly constant until $t = 300$ Myr. The bar is initially stronger in Run D, driving more gas to the centre. At late time, the evolution is similar for all runs, and the final values at $t = 1.5$ Gyr are proportional to the initial values of f_{gas} , differing by a factor of 2 between Runs D and H, and a factor of 2 between Runs H and J.

Figure 14 shows the AGN luminosity, vs. time, for Runs D, H, and J. As Figure 13 showed, reducing the gas fraction reduces the black hole mass M_{BH} . Since the Bondi accretion rate and the Eddington accretion rate both increase with M_{BH} , the AGN luminosity decreases with decreasing gas fraction. The peak luminosity is reached later for lower gas fractions, and once the peak is passed, the luminosity decreases slowly, for all runs, as the factor ρ_{∞} in equation (1) drops.

Figure 15 shows the evolution of the SFR, for Runs A, D, and G–J. The SFR drops significantly with gas fraction, both for galaxies with an AGN (solid lines) and without

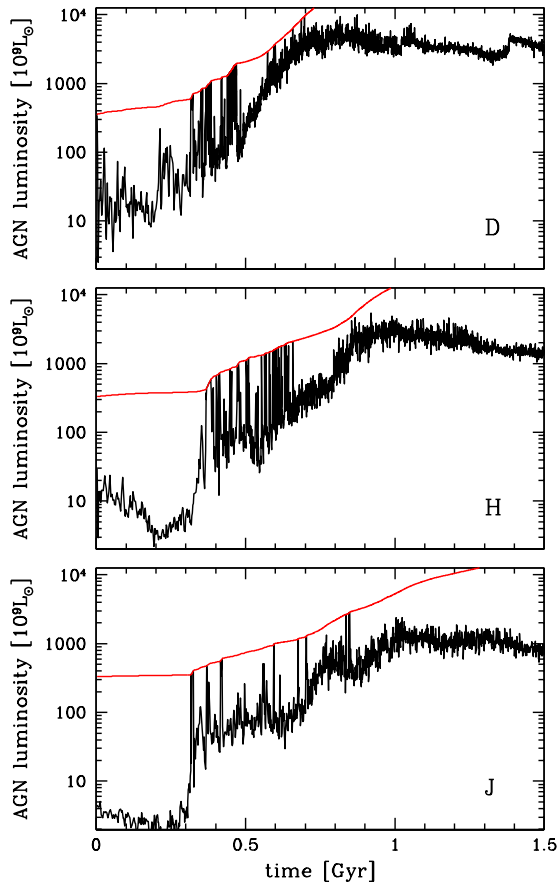


Figure 14. AGN luminosity vs. time for barred galaxies with $t_{\text{AGN}} = 0$ Gyr and $f_{\text{kin}} = 0.2$: Run D ($f_{\text{gas}} = 0.192$), Run H ($f_{\text{gas}} = 0.096$), and Run J ($f_{\text{gas}} = 0.048$), as indicated. The red lines show the Eddington luminosity.

(dotted lines). Not only the gas density is reduced in gas-poor galaxies, directly affecting star formation efficiently, but this reduction in density also increases the cooling time of the gas, since the cooling rate scales like the square of the density. This is reflected both in the global and the central SFR. With a lower gas fraction, the SFR rises slower, peaks at a lower value, and reaches this peak later. Comparing the bottom panel of Figure 15 with the top panel of Figure 12, we see that the central SFR closely follows the central gas mass.

Figures 16 and 17 show spacetime maps of the star formation history, for the entire galaxy and inside the central region, respectively, for Runs A, D, and G–J. Reducing the initial gas mass reduces star formation activity, particularly in the outer regions. Indeed, star formation in the outer regions is nearly absent in gas-very-poor galaxies. AGN feedback pushes star formation to larger radii (right column of Fig. 17). Lowering the gas fraction leads to competing effects: on one hand the AGN luminosity is lower, but on the other hand the more diffuse gas is more susceptible to AGN feedback. Going from Run D (gas-normal) to Run H (gas-poor), the nuclear star formation “cavity” gets bigger: star formation is pushed outward, indicating that the second effect dominates. Going from Run H (gas-poor) to Run J (gas-

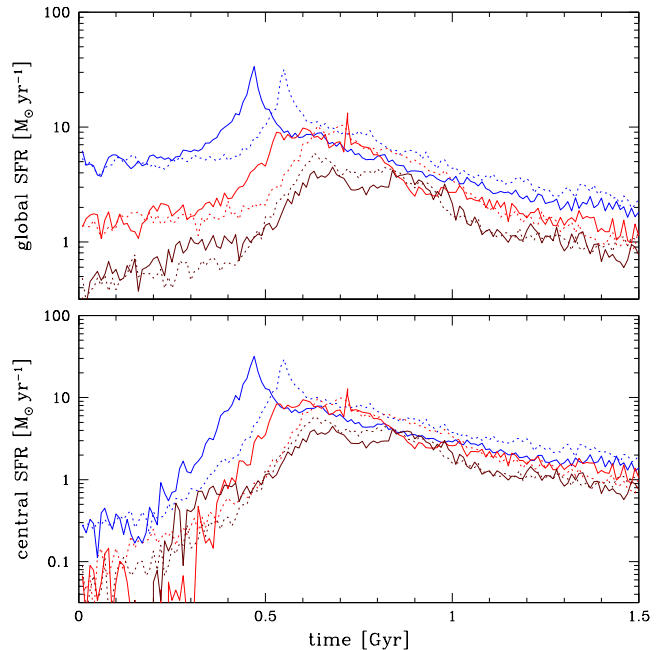


Figure 15. Star formation rate vs. time for galaxies with no AGN (dotted lines) and with AGN feedback ($f_{\text{kin}} = 0.2$, solid lines). Top panel: entire galaxy; bottom panel: central 1 kpc region. Blue lines: Runs A and D (gas-normal galaxies); red lines: Runs G and H (gas-poor galaxies); brown lines: Runs I and J (gas-very-poor galaxies).

very-poor), however, does not affect the location of central star formation very much, as the two effects mostly cancel each other.

5 DISCUSSION

We considered isolated disc galaxies in which the bar forms by instability. Other processes, such as mergers and tidal interactions, can also lead to the formation (or destruction) of a bar. In this study, we are focussing on the interplay between the bar and the AGN activity, and their impact on star formation, and not on the bar formation process itself. We see bar instability as a tool that enables us to numerically generate galaxies with bars. The alternative would have been to generate initial conditions in which the bar was already present, but this approach might produce initial conditions that are somewhat artificially unstable. By allowing the bar to form by instability, we ensure that the system is relaxed by the time the bar forms.

We discovered, somewhat surprisingly, that the bar strength A_2 reached its peak value earlier in simulations with AGN feedback. It appears that feedback speeds up the growth of bar instability, a phenomenon also noticed by Spinoso et al. (2017). The origin of this trend is certainly worth investigating further, but this is not the goal of the present study. In all simulations with bars, the peak values of A_2 are similar, and the post-peak evolution of A_2 is also similar. The differences between simulations do not result from different bar strengths. As long as we regard bar instability as a mere tool to generate initial conditions, the

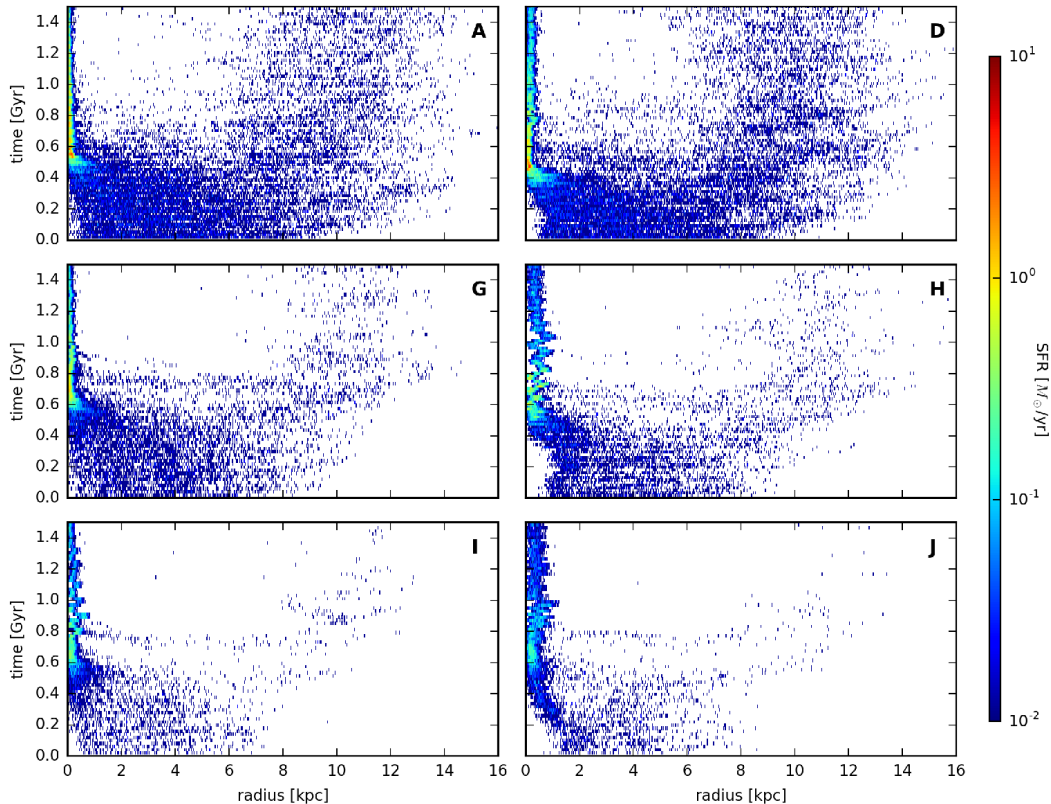


Figure 16. Star formation maps for gas-normal galaxies (top row), gas-poor galaxies (middle row), and gas-very-poor galaxies (bottom row), showing entire galaxy. Left column: with no AGN feedback. Right column: with AGN feedback ($f_{\text{kin}} = 0.2$).

pre-peak evolution of the bar is not relevant to this study, and we will postpone a detailed investigation of the effect of AGN feedback on bar instability to further work.

Since our goal was to assess the relative importance of positive and negative feedback, we were not interested in situations where AGN feedback blows all the gas outside of the galaxy. For this reason, we chose a regime of galaxy mass large enough for AGN feedback to dominate over SNe feedback, yet low enough to retain most of its gas. Also, our algorithm does not allow for the presence of anisotropic feedback (that is, jets), since the region near the black hole that would be responsible for making the ejecta anisotropic is not resolved by the algorithm. Still, our numerical models provide numerical experiments in the regime of relatively weak AGN feedback which only affects the central region of the galaxy. Our comparison of models with different AGN strengths, barred vs. unbarred galaxies, and different gas fractions provides qualitative trends of the effect of AGN feedback in the case of weak AGN feedback systems.

In all simulations with feedback, we use an AGN feedback model based on Wurster & Thacker (2013a). As noted by Barai et al. (2014), the Bondi accretion rate assumes a steady, adiabatic, spherically symmetric inflow, which is unlikely to be the case for a supermassive black hole, and that a more realistic accretion rate may differ from the Bondi accretion rate by orders of magnitude. Furthermore, the density at the Bondi radius is only resolved at high resolution, and so it is necessary to incorporate additional factors to correct

for this. Additionally, the angular momentum of the inflowing gas has an impact on the accretion rate (Powers et al. 2011; Wurster & Thacker 2013b), but this is difficult to capture at galaxy-scale and cosmological resolutions. Considering these uncertainties, we decided to base our algorithm on the WT model of Wurster & Thacker (2013a), because it is simple and numerically stable. Finally, we note that our AGN model produces luminosities of order $10^{12} L_{\odot}$ even in the later phase. This likely violates the number fraction of the luminous AGN in this type of galaxies. Therefore, our model overestimates the accretion rate in the late phase, and highlights that this is a challenge for current AGN models.

As in Papers I and II, we have only considered isolated galaxies, ignoring accretion from the intergalactic medium, and merger with other galaxies. These processes could affect the dynamics of the bar, and also affect the post-starburst evolution of barred galaxies, by replenishing the supply of gas depleted by star formation (see, however, Ellison et al. 2015a). Our simulations are most relevant to galaxies located at sufficiently low-redshift that most of the mass assembly is completed (e.g. L’Huillier et al. 2012). We will consider the effects of accretion and mergers in future work.

6 SUMMARY AND CONCLUSION

The goal of this study was to determine if AGN feedback has a positive or a negative effect on star formation in galaxies,

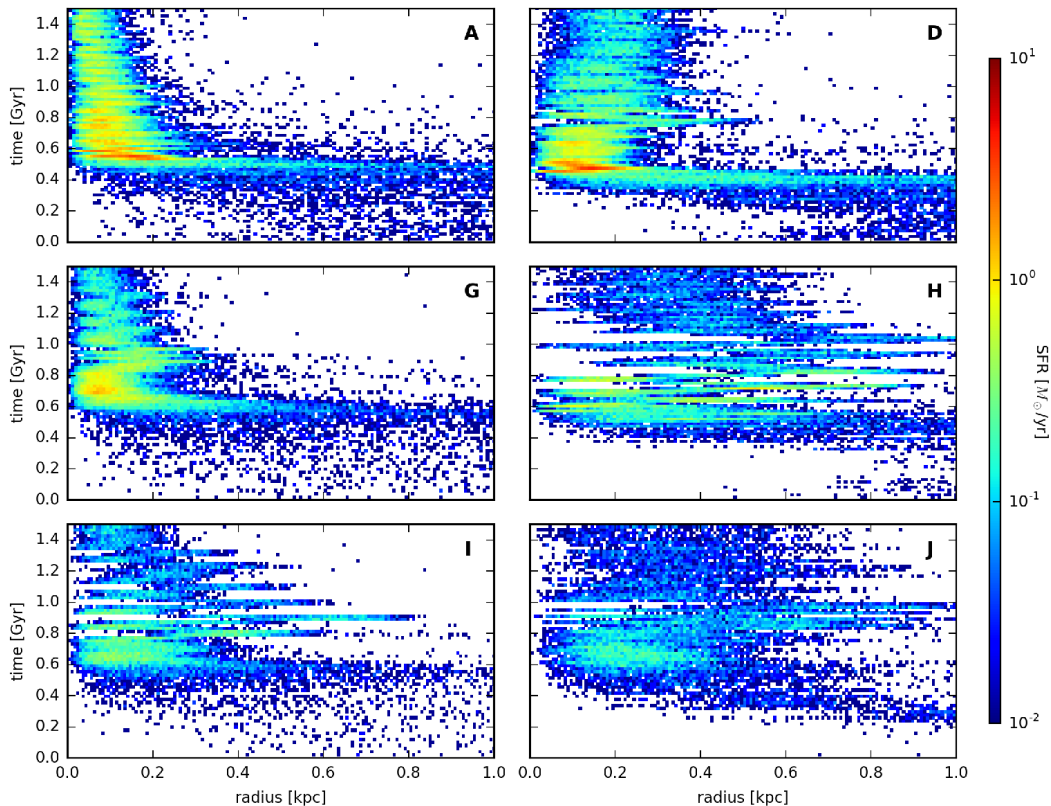


Figure 17. Star formation maps for gas-normal galaxies (top row), gas-poor galaxies (middle row), and gas-very-poor galaxies (bottom row), showing central 1 kpc region. Left column: with no AGN feedback. Right column: with AGN feedback ($f_{\text{kin}} = 0.2$).

in a regime of relatively weak AGN feedback which only affects the central regions of the galaxies. We have performed a series of 12 simulations of equal-mass barred and unbarred disc galaxies, with various initial gas fractions and various prescriptions for AGN feedback. We focussed on barred galaxies because of the ability of a bar to channel gas toward the centre of galaxies and feed an AGN. Our main results are the following:

- In all simulations, the bar forms and grows by instability. The presence of an AGN can hasten the onset of bar growth, and the bars reach their peak strength earlier. But eventually all bars settle to a similar strength, independent of AGN feedback prescription or initial gas fraction.

- AGN feedback initially has a strong positive effect on star formation. The SFR increases faster, and peaks earlier. In the central regions (smaller than 1 kpc), this difference can be attributed directly to AGN feedback. At larger radii, the difference results from delays in the formation of the bar. After most of the available gas has been converted into stars, the evolution of the SFR is essentially the same for all runs. Eventually, the SFR in simulations without feedback catches up, and at late time the total stellar mass is slightly larger than in simulations with feedback.

- The effect of AGN feedback is most important when it can act before star formation becomes significant. If the turn-on of AGN feedback is delayed until after star formation in the central region is well under way, the effect on the SFR is small.

- Feedback greatly affects the dynamics of the central region. In the absence of feedback, star formation peaks at the very centre of the galaxy, where the gas density is highest. Feedback pushes gas outward, where it supersonically collides with gas inflowing along the bar. As a result, star formation starts earlier, is more dramatic, and is pushed to larger radii.

- When the initial gas fraction is reduced, the formation of the bar is delayed. This in turn delays star formation and reduces the peak value of the SFR. The final values of the global and central stellar masses M_* decrease with decreasing initial gas fraction, and are hardly affected by AGN feedback.

- The bar plays a significant role in the evolution of the galaxies, by driving gas toward the centre where it can form stars and feed the AGN. By the end of the simulations, the black hole mass was lower by a factor of 30 and the central stellar mass was lower by a factor of more than 3 in unbarred galaxies compared to barred ones. Furthermore, the effect of AGN feedback in unbarred galaxies is negligible, except in the central 1 kpc region where star formation is suppressed. In particular, the global SFR is nearly identical in unbarred galaxies with and without feedback. Compared with barred galaxies, unbarred galaxies have a much lower AGN luminosity and the central region contains less gas that is susceptible to be affected by feedback.

Our final conclusion is that both positive and negative AGN feedback are present. Feedback suppresses star forma-

tion near the central black hole (negative feedback). The gas is pushed outward where it collides with inflowing gas, forming a dense ring in which star formation is enhanced (positive feedback). In barred galaxies, these two effects mostly cancel out. Stars form at different locations and times, but in a similar amount. In unbarred galaxies, negative feedback is more efficient and positive feedback is less efficient, leading to a net reduction of star formation. Our results are fully consistent with the analytical model proposed by Ishibashi & Fabian (2012).

ACKNOWLEDGMENTS

This research is supported by the Canada Research Chair program and NSERC. DJW is supported by European Research Commission grant ERC-StG-6771177 DUST-IN-THE-WIND.

REFERENCES

- Allen, S. W., Dunn, R. J. H., Fabian, A. C., Taylor, G. B., & Reynolds, C. S. 2006, *MNRAS*, 372, 21
- Alonso, S., Coldwell, G., & Lambas, D. G. 2014, *A&A*, 572, 86
- Arsenault, R. 1989, *A&A*, 217, 66
- Athanassoula, E. 1992, *MNRAS*, 259, 345
- Athanassoula, E., & Misiriotis, A. 2002, *MNRAS*, 330, 35
- Balmaverde, B., et al. 2016, *A&A*, 585, A148
- Bang, J., & Ann, H. B. 2009, *J. Korean Earth Sci. Soc.*, 30, 1
- Barai, P., Viel, M., Murante, G., Gaspari, M., & Borgani, S. 2014, *MNRAS*, 437, 1456
- Barkana, R., & Loeb, A. 2000, *ApJ*, 539, 20
- Barkana, R., & Loeb, A. 2006, *MNRAS*, 371, 395
- Barnes, D. J., Kawata, D., & Wu, K. 2012, *MNRAS*, 420, 3195
- Behroozi, P. S., Conroy, C., & Wechsler, R. H. 2010, *ApJ*, 717, 379
- Bekki, K. 2009, *MNRAS*, 339, 2221
- Bell, E. F., McIntosh, D. H., Katz, N., & Weinberg, M. D. 2003, *ApJ*, 585, L117
- Benítez-Llambay, A., Navarro, J. F., Abadi, M. G., Gottlöber, S., Yepes, G., Hoffman, Y., & Steinmetz, M. 2013, *ApJ*, 763, L41
- Benson, A. J., Bower, R. G., Frenk, C. S., Lacey, C. G., Baugh, C. M., & Cole, S. 2003, *ApJ*, 599, 38
- Best, P. N., & Heckman, T. M. 2012, *MNRAS*, 421, 1569
- Best, P. N., Kauffmann, G., Heckman, T. M., Brinchmann, J., Charlot, S., Ivezić, Z., & White, S. D. M. 2005, *MNRAS*, 362, 25
- Best, P. N., Kaiser, C. R., Heckman, T. M., & Kauffmann, G. 2006, *MNRAS*, 368, L67
- Bondi, H. 1952, *MNRAS*, 112, 195
- Bondi, H., & Hoyle, F. 1944, *MNRAS*, 104, 273
- Booth, C. M., & Schaye, J. 2009, *MNRAS*, 398, 53
- Bower, R. G., Benson, A. J., Malbon, R., Helly, J. C., Frenk, C. S., Baugh, C. M., Cole, S., Lacey, C. G. 2006, *MNRAS*, 370, 645
- Bower, R. G., Benson, A. J., & Crain, R. A. 2012, *MNRAS*, 422, 2816
- Capelo, P. R., Volonteri, M., Dotti, M., Belovary, J. M., Mayer, L., & Governato, F. 2015, *MNRAS*, 447, 2123
- Carles, C., Martel, H., Kawata, D., & Ellison, S. L. 2016, *MNRAS*, 463, 1074 (Paper II)
- Carniani, S. et al. 2016, *A&A*, 591, 28
- Cheung, E. et al. 2014, *MNRAS*, 447, 506
- Cisternas, M., Sheth, K., Salvato, M., Knapen, J. H., Civano, F., & Santini, P. 2015, *ApJ*, 802, 137
- Cole, S., et al. 2001, *MNRAS*, 326, 255
- Combes, F. 2003, in *ASP Conf. Ser. 209, Active Galactic Nuclei: From Central Engine to Host Galaxy*, eds. S. Collin, F. Combes, & I. Shlosman (San Francisco, CA: ASP), 441
- Combes, F., & Elmegreen, B. G. 1993, *A&A*, 271, 391
- Cox, T. J., Jonsson, P., Primack, J. R., & Somerville, R. S. 2006, *MNRAS*, 373, 1013
- Cresci, G. et al. 2015, *ApJ*, 799, 82
- Dalla Vecchia, C., & Schaye, J. 2008, *MNRAS*, 387, 1431
- Davé, R., Finlator, K., & Oppenheimer, B. D. 2006, *MNRAS*, 370, 273
- Duffy, A. R., Wyithe, J. S. B., Mutch, S. J., & Poole, G. B. 2014, *MNRAS*, 443, 3435
- Efstathiou, G. 2000, *MNRAS*, 317, 697
- Ellison, S. L., Nair, P., Patton, D. R., Scudder, J. M., Mendel, J. T., & Simard, L. 2011, *MNRAS*, 416, 2182
- Ellison, S. L., Fertig, D., Rosenberg, J. L., Nair, P., Simard, L., Torrey, P., & Patton, D. R. 2015a, *MNRAS*, 448, 221
- Ellison, S. L., Patton, D. R., & Hickox, R. C. 2015b, *MNRAS*, 451, L35
- Elmegreen, B. G. 2011, *ApJ*, 737, 10
- Emsellem, E., Greusard, D., Combes, F., Friedli, D. Leon, S., Pécontal, E., & Wozniak, H. 2001, *A&A*, 368, 52
- Falceta-Gonçalves, D. 2013, *MNRAS*, 432, 589
- Ferland, G. J., Korista, K. T., Verner, D. A., Ferguson, J. W., Kingdon, J. B., & Verner, E. M. 1998, *PASP*, 110, 761
- Ferrarese, L., & Merritt, D. 2000, *ApJ*, 539, L9
- Galloway, M. A. et al. 2015, *MNRAS*, 448, 3442
- Gaspari, M., Ruzszkowski, M., & Oh, S. P. 2013, *MNRAS*, 432, 3401
- Guo, Q., et al. 2011, *MNRAS*, 413, 101
- Gebhardt, K., et al. 2000, *ApJ*, 539, L13
- Germain, J., Barai, P., & Martel, H. 2009, *ApJ*, 704, 1002
- Gnedin, N. Y., & Kaurov, A. A. 2014, *ApJ*, 793, 30
- Grand, R. J. J., Kawata, D., & Cropper, M. 2015, *MNRAS*, 447, 4018
- Gültekin, K., et al. 2009, *ApJ*, 698, 198
- Hao, L., Jogee, S., Barazza, F. D., Marinova, I., & Shen J., 2009, in *ASP Conf. Ser. 419, Galaxy Evolution: Emerging Insights and Future Challenges*, eds. S. Jogee, I. Marinova, L. Hao., & G. A. Blanc (San Francisco, CA:ASP), 402
- Hardcastle, M. J., Evans, D. A., & Croton, J. H. 2006, *MNRAS* 370, 1893
- Hardcastle, M. J., Evans, D. A., & Croton, J. H. 2007, *MNRAS* 376, 1849
- Håring, N., & Rix, H.-W. 2004, *ApJ*, 604, L89
- Heller, C. H., & Shlosman, I. 1994, *ApJ*, 424, 84
- Ho, L. C., Filippenko, A. V., & Sargent, W. L. W. 1997, *ApJ*, 487, 591
- Hopkins, P. F., Quataert, E., & Murray, N. 2012, *MNRAS*, 421, 3488
- Hoyle, F., & Lyttleton, R. A. 1939, *proceedings of the Cam-*

- bridge Philosophical Society, 34, 405
- Hunt, L. K., & Malkan, M. A. 1999, *ApJ*, 516, 660
- Ishibashi, W., & Fabian, A. C. 2012, *MNRAS*, 427, 2998
- Iwamoto, K., Brachwitz, F., Nomoto, K., et al. 1999, *ApJSS*, 125, 439
- Jogee, S. 2006, in *Physics of Active Galactic Nuclei at all Scales*, eds. D. Alloin, R. Johnson, & P. Lira (Lecture Notes in Physics, Vol 693; Berlin:Springer), 143
- Jogee, S., Scoville, N., & Kenney, J. D. P. 2005, *ApJ*, 630, 837
- Johansson, P. H., Naab, T., & Burkert, A., 2009, *ApJ*, 690, 802
- Kauffmann, G., & Heckman, T. M. 2009, *MNRAS*, 346, 1055
- Kauffmann, G., et al. 2003, *MNRAS*, 346, 1055
- Kawata, D. & Gibson, B. K. 2003, *MNRAS*, 340, 908
- Kawata, D. & Gibson, B. K. 2005, *MNRAS*, 358, L16
- Kawata, D., Gibson, B. K., Barnes, D. J., Grand, R. J. J., & Rahimi, A. 2014, *MNRAS*, 438, 1208
- Kawata, D., & Mulchaey, J. S. 2008, *ApJ*, 672, L103
- Kawata, D., Okamoto, Gibson, B. K., Barnes, D. J., & Cen, R. 2013, *MNRAS*, 428, 1968
- Kirkman, D., Tytler, D., Suzuki, N., O’Meara, J. M., & Lubin, D. 2003, *ApJS*, 149, 1
- Knapen, J., H., Pérez-Ramírez, D., & Laine, S. 2002, *MNRAS*, 337, 808
- Knapen, J., H., Shlosman, I., & Peletier, R. F. 2000, *ApJ*, 529, 93
- Laine, S., Shlosman, I., Knapen, J. H., & Peletier, R. F. 2002, *ApJ*, 567, 97
- Laurikainen, E., Salo, H., & Buta, R. 2004, *ApJ*, 607, 103
- Lee, G.-H., Woo, J.-H., Lee, M. G., Hwang, H. S., Lee, J. C., Sohn, J. & Lee, J. H. 2012, *ApJ*, 750, 141
- L’Huillier, B., Combes, F., & Semelin, B. 2012, *A&A*, 544, A68
- Maciejewski, W. Teuben, P. J., Sparke, L. S., & Stone, J. M. 2002, *MNRAS*, 329, 502
- Marconi, A., & Hunt, L. K. 2003, *ApJ*, 589, L21
- Martel, H., Kawata, & Ellison, S. L. 2013, *MNRAS*, 431, 2560 (Paper I)
- Martinet, L., & Friedli, D. 1997, *A&A*, 323, 363
- Makiya, R., Totani, T., Kobayashi, M. A. R., Nagashima, M., & Takeuchi, T. T. 2014, *MNRAS*, 441, 63
- McConnell, N. J., & Ma, C.-P. 2013, *ApJ*, 764, 184
- McKee, C. F., & Ostriker, J. P. 1977, *ApJ*, 218, 148
- McLoed, K. K., & Rieke, G. H. 1995, *ApJ*, 441, 96
- McNaught-Roberts, T., et al. 2014, *MNRAS*, 445, 2125
- Mo H. J., Yang X., van den Bosch F. C., & Jing Y. P. 2004, *MNRAS*, 349, 205
- Moles, M., Marquez, I., & Perez, E. 1995, *ApJ*, 438, 604
- Moster, B. P., Somerville, R. S., Maulbetsch, C., et al. 2010, *ApJ*, 710, 903
- Muñoz, J. A., & Loeb, A. 2006, *ApJ*, 729, 99
- Mulchaey, J. S., & Regan, M. W. 1997, *ApJ*, 482, L135
- Navarro, J. F., Frenk, C. S., & White, S. D. M. 1996, *ApJ*, 462, 563
- Oh, S., Oh, K., and Yi, S. K. 2012, *ApJS*, 198, 4
- Pérez-González, P. G., et al. 2008, *ApJ*, 675, 234
- Pieri, M. M., & Martel, H. 2007, *ApJ*, 662, L7
- Pieri, M. M., Martel, H., & Grenon, C. 2007, *ApJ*, 658, 36
- Powers, C., Nayakshin, S., & King, A. 2001, *MNRAS*, 412, 269
- Puchwein, E., & Springel, V. 2013, *MNRAS*, 428, 2966
- Rahimi, A., & Kawata, D. 2012, *MNRAS*, 422, 2609
- Roos, O., Juneau, S., Bourneau, F., & Gabor, J. M. 2015, *ApJ*, 800, 19
- Salpeter, E. E. 1955, *ApJ*, 121, 161
- Salucci, P., & Persic, M. 1999, *MNRAS*, 309, 923
- Shakura, N. I., & Sunyaev, R. A. 1973, *A&A*, 24, 337
- Shen, S., Mo, H. J., White, S. D. M., et al. 2003, *MNRAS*, 343, 978
- Shlosman, I., Frank, J., & Begelman, M. C. 1989, *Nature*, 338, 45
- Shlosman, I., & Noguchi, M. 1993, *ApJ*, 414, 474
- Smolcic, V. 2009, *ApJ*, 699, L43
- Somerville R. S., Hopkins P. F., Cox T. J., Robertson B. E., & Hernquist L. 2008, *MNRAS*, 391, 481
- Spinoso, D., et al. 2017, *MNRAS*, 465, 3729
- Springel, V., Di Matteo, T., & Hernquist, L. 2005, *MNRAS*, 361, 776
- Tassis, K., Abel, T., Bryan, G. L., & Norman, M. L. 2003, *ApJ*, 587, 13
- Thacker, R. J., MacMackin, C., Wurster, J., & Hobbs, A. 2014, *MNRAS*, 443, 1125
- Veilleux, S., Cecil, G., & Bland-Hawthorn, J. 2005, *ARA&A*, 43, 769
- Wyithe, J. S. B., & Cen, R. 2007, *ApJ*, 659, 890
- Wyithe, J. S. B., & Loeb, A. 2006, *Nature*, 441, 322
- Woolley, S. E., & Weaver, T. A. 1995, *ApJSS*, 101, 181
- Wurster, J. & Thacker, R. J. 2013a, *MNRAS*, 431, 2513
- Wurster, J. & Thacker, R. J. 2013b, *MNRAS*, 431, 539
- Yoshida, N., Oh, S. P., Kitayama, T., & Hernquist, L. 2007, *ApJ*, 663, 687